

Modeling and Simulation of Surfactant Polymer Flooding using a New Hybrid Method

Prabir Daripa* and Sourav Dutta†

Department of Mathematics, Texas A&M University
College Station, TX 77843-3368

January 18, 2016

Abstract

Chemical enhanced oil recovery by surfactant-polymer flooding has been studied in two space dimensions. A two-phase porous media flow model has been proposed that incorporates the effect of capillary pressure and also the effect of polymer and surfactant on viscosity, interfacial tension and relative permeabilities of the two phases. A new global pressure for the two-phase, incompressible, immiscible, multicomponent porous media flow has been defined so that the equation for the global pressure remains same as the one for the pressure in the absence of the capillary pressure. This canonical form of the equation is solved more efficiently for the global pressure from which the phase pressures are easily recovered. The coupled system of equations for pressure, water saturation, polymer concentration and surfactant concentration is solved using a hybrid method in which the elliptic global pressure equation is solved using a discontinuous finite element method and the transport equations for water saturation and concentrations of the components are solved by a Modified Method Of Characteristics (MMOC). Numerical simulations have been performed to qualitatively validate the method and to evaluate the relative performance of various flooding schemes for several heterogeneous reservoirs.

Keywords: surfactant-polymer flooding, global pressure, capillary pressure, finite element method, method of characteristics, numerical simulations, heterogeneous permeability

1 Introduction

One of the effective methods of tertiary oil recovery is Surfactant-Polymer (SP) flooding which involves injection of polymer and surfactant laden aqueous phase in oil reservoirs. Polymer in the displacing fluid improves oil recovery by inhibiting the growth rate of the fingering instability and by increasing the water saturation level behind the displacing front. See Daripa et al. [1988a] for a study of these phenomena during polymer flooding which in general is a less effective method of tertiary oil recovery than the SP flooding, a subject of present study. In the SP flooding, use of surfactant further improves oil recovery by reducing the capillary pressure between the aqueous and the oil phases and by reducing the residual saturation limits of the rock matrix. ASP flooding in which Alkali is also used in the SP-laden aqueous phase is supposed to be even more effective since the Alkali produces surfactant in-situ thereby replenishing surfactant lost due to adsorption by the porous matrix during the transport of these chemical components by the flow through the porous matrix. In recent years, surfactant-polymer flooding has been shown to be preferable to even ASP flooding in highly heterogeneous reservoirs as the elimination of alkali removes undesirable inorganic scale formation, incompatibility with some polymers and demulsification difficulties ([Karazincir et al., 2011, Katsanis et al., 1983]). Therefore, the SP flooding is of significant current interest and is drawing a lot of attention ([Alsofi

* Author for correspondence (email:daripa@math.tamu.edu)
† email:sdutta@math.tamu.edu

et al., 2013, Gao et al., 2014, Thirawarapan et al., 2014, Wu et al., 2014, Yu et al., 2010, Zhenquan et al., 2012, Zhu et al., 2012]). Also visit the youtube link <https://www.youtube.com/watch?v=JqkNywPyBSw>

Various high-order accurate *finite difference methods* [Daripa et al., 1986, 1988a,b, Islam and Chakma, 1991, Shiyi et al., 1995] and locally mass conservative *finite volume methods* [Durlofsky, 1993, Healy and Russell, 1993] have been applied in the past for the numerical simulation of oil reservoirs. Various types of *finite element methods* such as control volume (CVFE), discontinuous (DG -[Bastian, 2003, Reed and Hill, 1973, Rivière and Wheeler, 2002]) and mixed [Nayagum et al., 2004] FE have also become a popular choice for the reservoir simulation because these methods do not suffer from much grid orientation effects, allow local grid refinement and have high order of accuracy. These methods are also versatile and have been applied to other problems such as simulation of faults and fractures. In problems where advection dominates diffusion, finite element methods have been found to exhibit excessive nonphysical oscillations for non-smooth solutions. Such nonphysical oscillations do not arise in characteristic based methods in which the advection is treated by a characteristic tracking approach. There are an abundance of such methods, for example see Douglas Jr and Russell [1982], Celia et al. [1990], Russell and Celia [2002], Wang et al. [1995], Arbogast and Wheeler [1995], Chen [2002], Douglas Jr et al. [2003, 1999, 2000].

In this paper, we propose a model that describes the displacement processes during the SP flooding and numerically solve the model using a new global pressure formulation and a non-traditional discontinuous finite element method in combination with the Modified Method Of Characteristics (MMOC) and time implicit methods to solve the system of the advection-diffusion equations for the concentrations of various phases and chemical components. To validate and show the performance of the method, we first use the simpler cases of waterflooding and polymer flooding and then go on to SP flooding as test problems for our method.

This paper is laid out as follows. In section 2, the global pressure formulations of the governing equations for polymer and SP flooding are derived and presented along with the various models of relative permeability and their dependence on the water saturation and concentrations of polymer and surfactant. In section 3, we present the numerical method: the computational grids, the non-traditional discontinuous finite element method, the MMOC for both polymer- and SP flooding, the construction of heterogeneity, and computational algorithm. We present and discuss the numerical results in section 4. Finally we conclude in section 5.

2 Mathematical model

2.1 Polymer flooding

Chemical EOR by polymer flooding process is usually modeled as an incompressible, immiscible, multi-component two-phase flow through porous media. Let Ω be a finite domain representing the porous reservoir with boundary $\partial\Omega$. Let the non-wetting phase (oil) and the wetting phase (water or an aqueous solution of polymer and/or surfactant) be denoted by the subscripts “ o ” and “ a ” respectively. Let s_j denote the saturation (volume fraction), \mathbf{v}_j denote the velocity, p_j denote the pressure and q_j denote the volumetric injection/production rate of phase j where $j = o$ or a . Then considering the hypothesis of capillary pressure and relative permeability we can write the following equations arising from the conservation of mass of each phase:

$$\phi \frac{\partial s_a}{\partial t} + \nabla \cdot \mathbf{v}_a = q_a, \quad (\mathbf{x}, t) \in \Omega \times (0, T] \quad (1a)$$

$$\phi \frac{\partial s_o}{\partial t} + \nabla \cdot \mathbf{v}_o = q_o, \quad (\mathbf{x}, t) \in \Omega \times (0, T]. \quad (1b)$$

The conservation of mass of the polymer dissolved in the aqueous phase gives rise to:

$$\phi \frac{\partial (c s_a)}{\partial t} + \nabla \cdot (c \mathbf{v}_a) = c_{inj} q_a, \quad (\mathbf{x}, t) \in \Omega \times (0, T], \quad (2)$$

where c is the concentration (volume fraction in the aqueous phase) of the dissolved polymer and it is assumed that the polymer is getting only passive advected with negligible diffusion. The conservation of momentum of each phase is given by the Darcy's law for each phase:

$$\mathbf{v}_a = -\mathbf{K}(\mathbf{x})\lambda_a \nabla p_a, \quad \mathbf{x} \in \Omega \quad (3a)$$

$$\mathbf{v}_o = -\mathbf{K}(\mathbf{x})\lambda_o \nabla p_o, \quad \mathbf{x} \in \Omega, \quad (3b)$$

which is coupled with the capillary pressure (p_c) equation for the immiscible phases:

$$p_c(s) = p_o - p_a. \quad (4)$$

We consider the porous medium to be initially saturated with the two phases and hence we get the equation:

$$s_o + s_a = 1. \quad (5)$$

Equation (5) implies that if eq. (1a) is solved for s_a , also written simply as s , then s_o can be easily obtained as $s_o = 1 - s$. The following initial and boundary conditions are prescribed.

$$s(\mathbf{x}) = s_0(\mathbf{x}) \quad \& \quad c(\mathbf{x}) = c_0(\mathbf{x}), \quad \mathbf{x} \in \Omega, \quad t = 0 \quad (6a)$$

$$\frac{\partial s}{\partial n} = 0, \quad \frac{\partial c}{\partial n} = 0 \quad \& \quad \mathbf{v}_j \cdot \hat{n} = 0, \quad \mathbf{x} \in \partial\Omega, \quad t > 0, \quad j = a, o \quad (6b)$$

Here is a list of the notations used:

- ϕ and $\mathbf{K}(\mathbf{x})$ are the porosity (taken to be constant in this study) and the permeability of the porous medium,
- $\lambda_j(s, c) = k_{rj}(s)/\mu_j(c)$, is the phase mobility where k_{rj} is the relative permeability and μ_j is the viscosity of phase j ,
- $\lambda = \lambda_a(s, c) + \lambda_o(s, c)$ is the total mobility,
- $\mathbf{v} = \mathbf{v}_a + \mathbf{v}_o$ is the total velocity.

The combination of the above equations describe the flow and transport problem in the phase pressure formulation which is a system of strongly coupled non-linear equations. This system is also degenerate as the eqs. (3a) and (3b) vanish at extreme values of the saturation s of the aqueous phase where the phase pressures p_a and p_o have no meaning. For these and many other reasons, mathematical and numerical studies of this problem including numerical simulations are very challenging. In order to avoid this difficulty, we propose a new global pressure formulation for incompressible, immiscible two-phase flows with dissolved components. The procedure is described below, in brief.

We observe the following identity:

$$\mathbf{v}_a = \frac{\lambda_o}{\lambda} \mathbf{v}_a - \frac{\lambda_a}{\lambda} \mathbf{v}_o + \frac{\lambda_a}{\lambda} (\mathbf{v}_o + \mathbf{v}_a) \quad (7)$$

Substituting eq. (7) in eq. (1a) we get,

$$\phi \frac{\partial s}{\partial t} - \nabla \cdot \left\{ \mathbf{K}(\mathbf{x}) \frac{\lambda_o}{\lambda} \lambda_a \nabla p_a - \mathbf{K}(\mathbf{x}) \frac{\lambda_a}{\lambda} \lambda_o \nabla p_o \right\} + \nabla \cdot \left\{ \frac{\lambda_a}{\lambda} (\mathbf{v}) \right\} = q_a,$$

or equivalently,

$$\phi \frac{\partial s}{\partial t} + \nabla \cdot \{ \mathbf{K}(\mathbf{x}) f(s, c) \lambda_o \nabla (p_c(s)) \} + \nabla \cdot (f(s, c) \mathbf{v}) = q_a. \quad (8)$$

Here $f(s, c) = \lambda_a(s, c)/\lambda(s, c)$ is the fractional flow function of the aqueous phase. Equation (8) is called the saturation equation. Next we define the global pressure, p , as

$$p = \frac{1}{2}(p_o + p_a) + \frac{1}{2} \int_{s_c}^s \left(\hat{\lambda}_o(\zeta, c) - \hat{\lambda}_a(\zeta, c) \right) \frac{dp_c}{d\zeta}(\zeta) d\zeta - \frac{1}{2} \int \left(\int_{s_c}^s \frac{\partial}{\partial c} \left(\hat{\lambda}_o(\zeta, c) - \hat{\lambda}_a(\zeta, c) \right) \frac{dp_c}{d\zeta}(\zeta) d\zeta \right) \left(\frac{\partial c}{\partial x} dx + \frac{\partial c}{\partial y} dy \right) \quad (9)$$

where $\hat{\lambda}_j = \lambda_j/\lambda$ for $j = a, o$ and s_c is the value of the aqueous phase saturation at which $p_c(s_c) = 0$. Taking gradients on both sides of eq. (9) and simplifying we obtain

$$\nabla p = \nabla \Psi - \frac{1}{2} \left(\int_{s_c}^s \frac{\partial}{\partial c} \left(\hat{\lambda}_o(\zeta, c) - \hat{\lambda}_a(\zeta, c) \right) \frac{dp_c}{d\zeta}(\zeta) d\zeta \right) \nabla c, \quad (10)$$

where

$$\Psi = \frac{1}{2}(p_o + p_a) + \frac{1}{2} \int_{s_c}^s (\hat{\lambda}_o(\zeta, c) - \hat{\lambda}_a(\zeta, c)) \frac{dp_c}{d\zeta}(\zeta) d\zeta \quad (11)$$

is the global pressure [Chavent and Jaffre', 1986] for incompressible, immiscible, two-phase flows without any dissolved component. Using eqs. (10) and (11) we obtain

$$\nabla p = \frac{1}{2} \nabla(p_o + p_a) + \frac{1}{2} (\hat{\lambda}_o(s, c) - \hat{\lambda}_a(s, c)) \nabla p_c(s). \quad (12)$$

Multiplying both sides of eq. (12) with $\mathbf{K}(\mathbf{x})\lambda$ and simplifying we get

$$-\mathbf{K}(\mathbf{x})\lambda \nabla p = \mathbf{v}. \quad (13)$$

Due to the incompressibility of the liquid phases we have

$$\nabla \cdot \mathbf{v} = q_a + q_o = \tilde{q}. \quad (14)$$

Using eq. (13) in eq. (14) we finally get

$$-\nabla \cdot (\mathbf{K}(\mathbf{x})\lambda(s, c)\nabla p) = \tilde{q}. \quad (15)$$

Equation (15) is the global pressure equation. Solving this equation (see below) yields the global pressure p from which the phase pressures p_a and p_o are easily recovered using the definition (4) for the capillary pressure and the definition (9) for the global pressure.

In summary, the complete system of governing equations for the polymer flooding process is given by:

$$-\nabla \cdot (\mathbf{K}(\mathbf{x})\lambda(s, c)\nabla p) = \tilde{q} \equiv \sum_i \tilde{q}^{(i)} \delta(\mathbf{x} - \mathbf{x}^{(i)}), \quad \mathbf{x} \in \Omega, t \in (0, T] \quad (16a)$$

$$\phi s_t + \nabla \cdot (\mathbf{v} f(s, c)) + \nabla \cdot (D \nabla p_c(s)) = q_a, \quad \mathbf{x} \in \Omega, t \in (0, T] \quad (16b)$$

$$\phi(s)_t + \nabla \cdot (\mathbf{v} c f(s, c)) + \nabla \cdot (D \nabla p_c(s)) = c_{inj} q_a, \quad \mathbf{x} \in \Omega, t \in (0, T] \quad (16c)$$

where $D(s, c) = \mathbf{K}(\mathbf{x})\lambda_o(s)f(s, c)$ and the initial and boundary conditions given by eqs. (6a) and (6b) are prescribed. It is to be noted that $\tilde{q} = q_o + q_a$ is an appropriate source term for the pressure equation which denotes the sum of the volumes of fluid of the oleic phase (q_o) and the aqueous phase (q_a) injected per unit volume per unit time. Numerically however, instead of modeling distributed mass sources or sinks we approximate the sources and sinks of the individual fluids to be located at a finite number of isolated points $\mathbf{x}^{(i)}$. Hence for point sources we define $\tilde{q}^{(i)}$ to be the total volume of fluids of both the phases injected per

unit volume per unit time at the point $\mathbf{x}^{(i)}$ so that $\tilde{q} = \Sigma_i \tilde{q}^{(i)} \delta(\mathbf{x} - \mathbf{x}^{(i)})$. We also make the following practical and physical assumptions:

$$q_a = \tilde{q} \quad \text{and} \quad q_o = 0 \quad \text{when } \tilde{q} \geq 0, \quad (17)$$

$$q_a = \lambda_a \tilde{q} \quad \text{and} \quad q_o = \lambda_o \tilde{q} \quad \text{when } \tilde{q} < 0, \quad (18)$$

which means that oil is never injected and the fluid mixture obtained at the production well is proportional to the resident fluid at that point. For the current study all the numerical experiments have been carried out in a two dimensional horizontal domain, $\Omega \in \mathbb{R}^2$ so that gravity terms can be neglected and we can focus on other complex physical and chemical phenomena.

The dependence of the relative permeabilities, k_{ra} and k_{ro} , and the capillary pressure on the saturation is obtained by using the Van Genuchten model [van Genuchten, 1980] and the subsequent generalization done by Parker [Parker et al., 1987].

$$k_{ra}(s) = s^{1/2} \left(1 - (1 - s^{1/m})^m\right)^2, \quad (19a)$$

$$k_{ro}(s) = s^{1/2} \left(1 - (1 - s^{1/m})^m\right)^{2m}, \quad (19b)$$

$$p_c(s) = \frac{1}{\alpha_0} \left(s^{-1/m} - 1\right)^{1-m}. \quad (19c)$$

The saturation at which the relative permeability goes to zero is referred to as the residual saturation. In eqs. (19a)–(19c) the residual wetting phase saturation, s_{ra} and non-wetting phase saturation, s_{ro} have been taken to be zero with the parameters $m = 2/3$ and $\alpha_0 = 0.125$ [Ghanbarian-Alavijeh et al., 2010]. It is to be noted that these parameter values depend on the interfacial tension between oil and water phases, σ_0 . Alternatively Corey-type imbibition relations can also be used, ([Brooks and Corey, 1966] and [Corey, 1986]):

$$\begin{aligned} k_{ra} &= \left(\frac{s - s_{ra}^{\sigma_0}}{1 - s_{ra}^{\sigma_0}}\right)^{3.5}, \\ k_{ro} &= \left(1 - \frac{s - s_{ra}^{\sigma_0}}{1 - s_{ra}^{\sigma_0} - s_{ro}^{\sigma_0}}\right)^2 \left[1 - \left(\frac{s - s_{ra}^{\sigma_0}}{1 - s_{ra}^{\sigma_0} - s_{ro}^{\sigma_0}}\right)^{1.5}\right], \end{aligned} \quad (20)$$

where k_{ra} and k_{ro} are the relative permeability functions of the aqueous phase and the oleic phase respectively when the interfacial tension between the two phases is given by σ_0 .

2.2 Surfactant-polymer flood

Surfactants have at least one hydrophobic group and one hydrophilic group in the same molecule. This dual character allows them to sufficiently lower the interfacial tension and also remarkably alter the wetting properties and hence they are considered as suitable agents in enhanced oil recovery processes. SP flooding is the process where a suitable combination of a surfactant and a polymer is mixed with water and the reservoir is flooded with this SP laden aqueous solution. This can achieve a higher level of oil recovery than polymer flood and become more economical if optimum quantities of all the agents are used. With the presence of surfactant, some of the parameters become dependent on the concentration of the surfactant, Γ . These are listed here.

- Phase mobilities : $\lambda_o(s, \Gamma) = k_{ro}(s, \Gamma)/\mu_o$ and $\lambda_a(s, c, \Gamma) = k_{ra}(s, \Gamma)/\mu_a(c)$.
- Total mobility : $\lambda(s, c, \Gamma) = \lambda_o(s, c, \Gamma) + \lambda_a(s, c, \Gamma)$.
- Fractional flow function : $f(s, c, \Gamma) = \lambda_a(s, c, \Gamma)/\lambda(s, c, \Gamma)$.

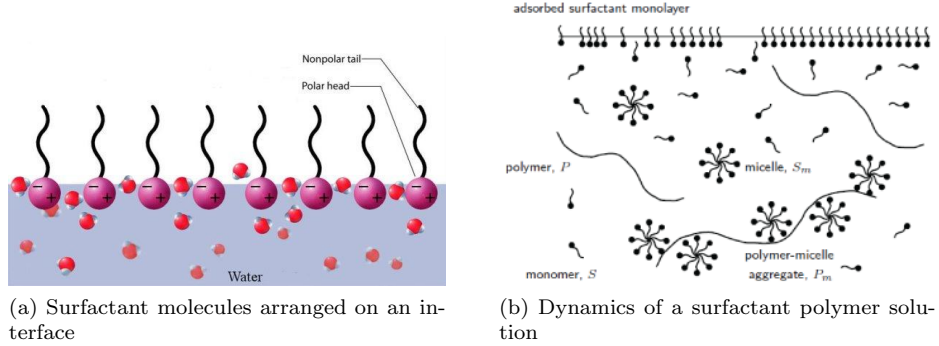


Figure 1: Pictorial representation of the rheology and behavior of surfactant molecules (a) near an interface and (b) in a solution containing dissolved polymer.

- Capillary Pressure : $p_c = p_c(s, \Gamma)$.

In order to redefine the global pressure for the case of SP flooding, we define the following:

$$\begin{aligned}\eta^c(s, c, \Gamma) &= \int_{s_c}^s \frac{\partial}{\partial c} (\hat{\lambda}_o - \hat{\lambda}_a)(\zeta, c, \Gamma) \frac{dp_c}{d\zeta}(\zeta, \Gamma) d\zeta + \int_{\Gamma_c}^\Gamma \frac{\partial}{\partial c} (\hat{\lambda}_o - \hat{\lambda}_a)(s, c, \xi) \frac{dp_c}{d\xi}(s, \xi) d\xi \\ \eta^s(s, c, \Gamma) &= \int_{\Gamma_c}^\Gamma \frac{\partial}{\partial s} (\hat{\lambda}_o - \hat{\lambda}_a)(s, c, \xi) \frac{dp_c}{d\xi}(s, \xi) d\xi \\ \eta^\Gamma(s, c, \Gamma) &= \int_{s_c}^s \frac{\partial}{\partial \Gamma} (\hat{\lambda}_o - \hat{\lambda}_a)(\zeta, c, \Gamma) \frac{dp_c}{d\zeta}(\zeta, \Gamma) d\zeta.\end{aligned}$$

Using the above definitions, the global pressure is defined similarly as before :

$$\begin{aligned}p &= \frac{1}{2}(p_o + p_a) + \frac{1}{2} \int_{s_c}^s (\hat{\lambda}_o - \hat{\lambda}_a)(\zeta, c, \Gamma) \frac{dp_c}{d\zeta}(\zeta, \Gamma) d\zeta + \frac{1}{2} \int_{\Gamma_c}^\Gamma (\hat{\lambda}_o - \hat{\lambda}_a)(s, c, \xi) \frac{dp_c}{d\xi}(s, \xi) d\xi \\ &\quad - \frac{1}{2} \int \eta^c(s, c, \Gamma) \left(\frac{\partial c}{\partial x} dx + \frac{\partial c}{\partial y} dy \right) - \frac{1}{2} \int \eta^s(s, c, \Gamma) \left(\frac{\partial s}{\partial x} dx + \frac{\partial s}{\partial y} dy \right) \\ &\quad - \frac{1}{2} \int \eta^\Gamma(s, c, \Gamma) \left(\frac{\partial \Gamma}{\partial x} dx + \frac{\partial \Gamma}{\partial y} dy \right) + C\end{aligned}\tag{21}$$

where as before $\hat{\lambda}_i(s, c, \Gamma) = \lambda_i(s, c, \Gamma)/\lambda(s, c, \Gamma)$ is the normalized mobility of phase i and C is a reference pressure which takes the place of an integration constant in the calculations. The above definition leads to

$$\nabla p = \frac{1}{2} \nabla(p_o + p_a) + \frac{1}{2} (\hat{\lambda}_o - \hat{\lambda}_a)(s, c, \Gamma) \nabla p_c(s, \Gamma)$$

which is analogous to the form of eq. (13). Hence the new system of equations for the surfactant-polymer model in non-conservative form is :

$$-\nabla \cdot (\mathbf{K}(\mathbf{x}) \lambda(s, c, \Gamma) \nabla p) = \tilde{q}, \tag{22a}$$

$$\phi \frac{\partial s}{\partial t} + \frac{\partial f}{\partial s} \mathbf{v} \cdot \nabla s + \nabla \cdot \left(\tilde{D} \frac{\partial p_c}{\partial s} \nabla s \right) = g_1 - \frac{\partial f}{\partial c} \mathbf{v} \cdot \nabla c - \frac{\partial f}{\partial \Gamma} \mathbf{v} \cdot \nabla \Gamma - \nabla \cdot \left(\tilde{D} \frac{\partial p_c}{\partial \Gamma} \nabla \Gamma \right), \tag{22b}$$

$$\phi \frac{\partial c}{\partial t} + \left(\frac{f}{s} \mathbf{v} + \frac{\tilde{D}}{s} \frac{\partial p_c}{\partial s} \nabla s + \frac{\tilde{D}}{s} \frac{\partial p_c}{\partial \Gamma} \nabla \Gamma \right) \cdot \nabla c = \frac{1}{s} (g_2 - c g_1), \tag{22c}$$

$$\phi \frac{\partial \Gamma}{\partial t} + \left(\frac{f}{s} \mathbf{v} + \frac{\tilde{D}}{s} \frac{\partial p_c}{\partial s} \nabla s + \frac{\tilde{D}}{s} \frac{\partial p_c}{\partial \Gamma} \nabla \Gamma \right) \cdot \nabla \Gamma = \frac{1}{s} (g_3 - \Gamma g_1), \tag{22d}$$

where Γ is the concentration of the surfactant mixed in the aqueous phase, $\tilde{D}(s, c, \Gamma) = \mathbf{K}(\mathbf{x})\lambda_o(s, c, \Gamma)f(s, c, \Gamma)$ and $g_1 = q_a$, $g_2 = c_{inj}q_a$, $g_3 = \Gamma_{inj}q_a$. Equation (22d) arises from the mass conservation law for the surfactant.

Capillary pressure is strongly dependent on the surfactant concentration. It reduces steadily with increasing surfactant concentration upto the CMC (Critical Micelle Concentration) due to the reduction in interfacial tension (IFT). The relationship of IFT with surfactant concentration has been extensively studied experimentally and is known to be inversely proportional in nature (Fig. 2). In order to model this complex dependence of capillary pressure on s as well as on Γ , we adopt the approach [Brown and Pope, 1994] that is often followed in SEAR (Surfactant Enhanced Aquifer Remediation) processes and it is given by the following empirical relation:

$$\left(\frac{p_b}{p_c}\right)^{\omega_1} = \left(1 - \frac{s - s_{ra}^\sigma}{1 - s_{ra}^\sigma - s_{ro}^\sigma}\right). \quad (23)$$

In the above, s_{ri}^σ ($i = a, o$) are the residual saturations for the aqueous and oleic phases respectively at interfacial tension σ , ω_1 is a curve fitting parameter called the pore-size index and p_b , often called the entry pressure, is a function of the interfacial tension between the two phases, which is expressed using a Leverett-J type function given by $p_b = \sigma\omega_2\sqrt{\phi/K}$ with ω_2 being a proportionality constant. Thus p_b implicitly captures the relationship between capillary pressure p_c and surfactant concentration Γ via the interfacial tension $\sigma = \sigma(\Gamma)$.

From surface chemistry we know that surfactants improve the mobilization of trapped oil by reducing the interfacial tension forces which in turn leads to the reduction of capillary pressure between oil and water. But this also leads to a reduction of residual oil saturation and hence an increase in the relative permeabilities of the two phases. In fact, for IFT values below 0.1 mN/m (milli Newton per meter) the relative permeabilities of both phases increase substantially due to a decrease of the residual saturations of the two phases with an increase in IFT (captured through the capillary number, N_c). This effect on the relative permeabilities and residual saturations can be captured through the relative permeability curves. In the current study, the relative permeability curves are modeled following the approach of [Amaefule and Handy, 1982] as:

$$k_{ra}^\sigma = \left(\frac{s - s_{ra}^\sigma}{1 - s_{ra}^\sigma}\right) \left\{ 2.5s_{ra}^\sigma \left[\left(\frac{s - s_{ra}^\sigma}{1 - s_{ra}^\sigma}\right)^2 - 1 \right] + 1 \right\},$$

$$k_{ro}^\sigma = \left(1 - \frac{s - s_{ra}^\sigma}{1 - s_{ra}^\sigma - s_{ro}^\sigma}\right) \left\{ 5s_{ro}^\sigma \left[\left(1 - \frac{s - s_{ra}^\sigma}{1 - s_{ra}^\sigma - s_{ro}^\sigma}\right) - 1 \right] + 1 \right\}. \quad (24)$$

Here k_{ra}^σ and k_{ro}^σ are the respective relative permeabilities of the aqueous and the oleic phases at an interfacial tension of σ . As before, s_{ra}^σ and s_{ro}^σ are the residual saturations of the aqueous phase and the oleic phase at interfacial tension σ , respectively.

To use the above models for the capillary pressure, eq. (23), and the relative permeability, eq. (24), we need to be able to determine the variation in the residual saturations of the phases with changes in the interfacial tension. For this purpose, we use the empirical expressions that relate the IFT and the residual saturations using the capillary number (see [Amaefule and Handy, 1982]) given as follows

$$s_{ro}^\sigma = \begin{cases} s_{ro}^{\sigma 0} & N_c < N_{co} \\ s_{ro}^{\sigma 0} \left(\frac{N_{co}}{N_c}\right)^{0.5213} & N_c \geq N_{co} \end{cases}, \quad (25)$$

$$s_{ra}^\sigma = \begin{cases} s_{ra}^{\sigma 0} & N_c < N_{cao} \\ s_{ra}^{\sigma 0} \left(\frac{N_{cao}}{N_c}\right)^{0.1534} & N_c \geq N_{cao} \end{cases}. \quad (26)$$

Here the exponents are obtained through curve fitting on experimental data. $N_c = \frac{\mu|\mathbf{v}|}{\sigma}$ is the capillary number calculated from the displacing fluid viscosity μ , Darcy velocity \mathbf{v} and interfacial tension, σ . N_{co} and

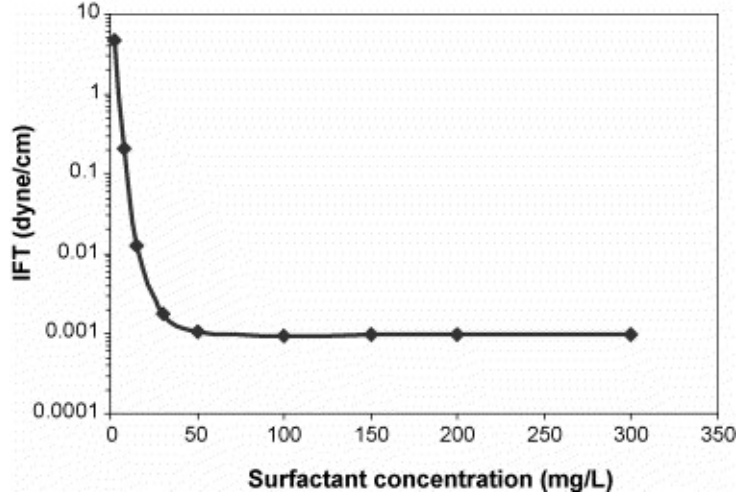


Figure 2: Interfacial tension of oil/brine as a function of surfactant concentration

N_{cao} are the oleic and the aqueous phase capillary numbers at interfacial tension, σ_0 , respectively. Finally to complete the model we assume an empirical relationship between the surfactant concentration and the interfacial tension that closely resembles the behavior observed in laboratory experiments (see [Liu et al., 2007]),

$$\sigma = \frac{10.001}{\Gamma + 1} - 0.001. \quad (27)$$

3 Numerical method

3.1 Computational grid

For our domain we consider the quarter five-spot test case which consists of a repeated pattern of squares. In each square there is an injection(+) well at the center and production(−) wells at the corners. Using the symmetry of the problem we consider one quarter of this square domain as our characteristic domain and normalize it to $\Omega = [0, 1]^2$ with an injection well (point source) at $(0, 0)$ and a production well (point sink) at $(1, 1)$. In order to solve the system of coupled transport equations given by eqs. (16b) and (16c) we partition the domain Ω into rectangular cells. Given positive integers $I, J \in \mathbb{Z}^+$, set $\Delta x = (x_{max} - x_{min})/I = 1/I$ and $\Delta y = (y_{max} - y_{min})/J = 1/J$. We define a uniform Cartesian grid $(x_i, y_j) = (i\Delta x, j\Delta y)$ for $i = 0, \dots, I$ and $j = 0, \dots, J$. Each (x_i, y_j) is called a grid point. For the case $i = 0, I$ or $j = 0, J$, a grid point is called a boundary point, otherwise it is called an interior point. The grid size is defined as $h = \max(\Delta x, \Delta y) > 0$, see Figure 3(a).

In order to solve the elliptic flow equation eq. (16a) for global pressure, we introduce triangulations inside the grid generated for the transport equations eqs. (16b) and (16c). This means every rectangular region $[x_i, x_{i+1}] \times [y_j, y_{j+1}]$ is cut into two pieces of right triangular regions: one is bounded by $x = x_i, y = y_j$ and $y = \frac{y_{j+1}-y_j}{x_{i+1}-x_i}(x - x_{i+1}) + y_j$, the other is bounded by $x = x_{i+1}, y = y_{j+1}$ and $y = \frac{y_{j+1}-y_j}{x_{i+1}-x_i}(x - x_{i+1}) + y_j$. Collecting all those triangular regions, also called elements, we obtain a uniform triangulation, $L^h = \{\kappa | \kappa \text{ is a triangular element}\}$, see Figure 3(b). We can also choose the hypotenuse to be $y = \frac{y_{j+1}-y_j}{x_{i+1}-x_i}(x - x_i) + y_j$, and get another uniform triangulation from the same Cartesian grid. There is no conceptual difference on these two triangulations for our method.

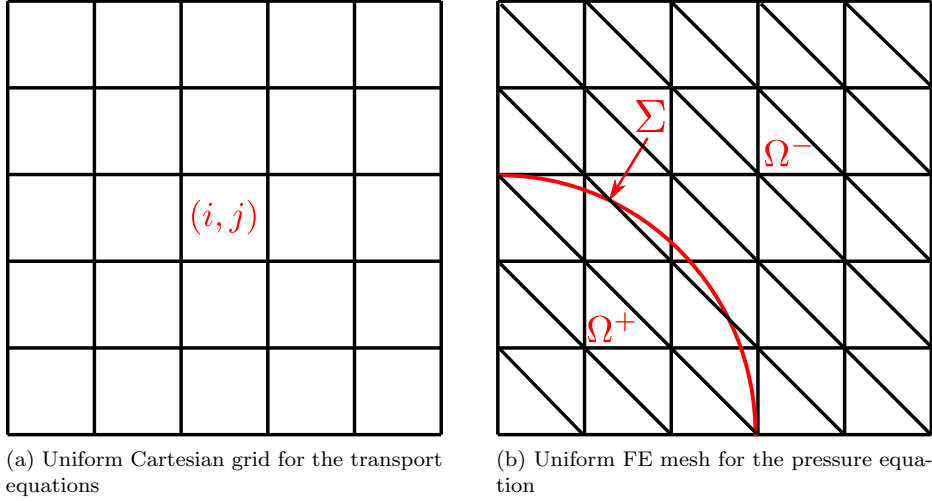


Figure 3: Discretization of the computational domain for the (a) Transport Equations and the (b) Pressure Equation.

3.2 Pressure equation

The elliptic equation is:

$$-\nabla \cdot (\mathbf{K}(\mathbf{x})\lambda(s, c)\nabla p) = \tilde{q}, \quad \mathbf{x} \in \Omega \setminus \Sigma, \quad (28a)$$

$$(\mathbf{K}(\mathbf{x})\lambda(s, c)\nabla p) \cdot \hat{\mathbf{n}} = 0, \quad \mathbf{x} \in \partial\Omega, \quad (28b)$$

where Σ denotes the union of the interfaces that separate Ω into several subdomains. In reality, there aren't any such continuous physical interfaces going through the porous rock matrix, but this is just a macroscopic averaged picture. Also, at any arbitrary time during the flooding process, there might be many such interfaces in the domain generated dynamically due to the flow and hence there can be several subdomains created inside Ω . However, for simplicity of exposition, here we assume that we have only two separated subdomains, Ω^+ and Ω^- . It is to be noted that at time $t = 0$, we begin with the ideal case of two subdomains separated by a single interface.

This problem is solved using a non-traditional finite element formulation (see [Hou et al., 2010]) with an uniform triangulated non-body-fitted grid which is second order accurate in the L^∞ norm for matrix coefficient elliptic equations with discontinuities across the interfaces. We prescribe the following kinematic condition at the interface Σ

$$[\mathbf{K}(\mathbf{x})\lambda(s, c)\Gamma]\nabla p \cdot \hat{\mathbf{n}}|_{\Sigma} = 0, \quad (29)$$

where $\hat{\mathbf{n}}$ is the outward unit normal which points from Ω^- to Ω^+ . We assume the boundary $\partial\Omega$ and the interface Σ to be Lipschitz continuous. Hence a unit normal vector, $\hat{\mathbf{n}}$ can be defined a.e. on Σ . We generalize the weak formulation for the elliptic equation in the usual Sobolev spaces $H^1(\Omega)$ with $\psi \in H^1(\Omega)$ as

$$\int_{\Omega^+} \mathbf{K}\lambda \nabla p \nabla \psi + \int_{\Omega^-} \mathbf{K}\lambda \nabla p \nabla \psi - \int_{\partial\Omega} \mathbf{K}\lambda \psi \nabla p \cdot \hat{\mathbf{n}} = \int_{\Omega} f \psi \quad (30)$$

where f denotes the point source term.

The elements, κ of triangulation, L^h , are classified into regular cells and interface cells. We call κ a regular cell if its vertices are in the same subdomain and an interface cell when its vertices belong to different subdomains. For an interface cell, $\kappa = \kappa^+ \cup \kappa^-$ where κ^+ and κ^- are separated by a line segment Σ_k^h , obtained by joining the two points where the interface Σ intersects the sides or the vertices of that interface

cell. A set of grid functions, $H^{1,h} = \{\omega^h \mid \omega^h = \omega_{i,j}; 0 \leq i \leq I, 0 \leq j \leq J\}$ are defined on the grid points of the mesh L^h . An extension operator $U^h : H^{1,h} \rightarrow H^1(\kappa)$ is constructed as follows. For any $\phi^h \in H^{1,h}$, $U^h(\phi^h)$ is a piecewise linear function and matches ϕ^h on the grid points. In a regular cell, it is a linear function that interpolates the values of ϕ^h at the grid points. In an interface cell, it consists of two pieces of linear functions, one each defined on κ^+ and κ^- . The location of the discontinuity of the extended function $U^h(\phi^h)$ in an interface cell is on the line segment Σ_k^h . Hence an interface jump condition on the pressure, p , if there is one, can be imposed on the two end points of this line segment at $\{\partial\kappa\} \cap \{\Sigma_k^h\}$ while the interface jump condition, eq. (29), is imposed at the middle point of Σ_k^h . The construction of such extension operators and proof of their uniqueness can be found in the literature [Li et al., 2003, Liu et al., 2000, Hou et al., 2010].

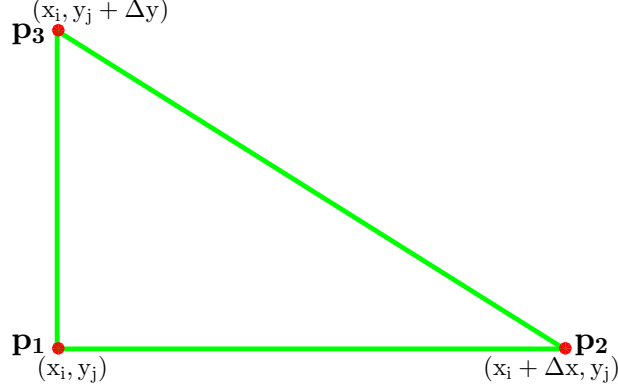


Figure 4: Regular cell

For every $\phi^h \in H^{1,h}$, we can define an unique extension $U^h(\phi^h)$ from knowing the position of the interface Σ . For a regular cell, as in Figure 4 we construct $U^h(\phi^h)$ as

$$U^h(\phi^h) = \phi(p_1) + \frac{\phi(p_2) - \phi(p_1)}{\Delta x}(x - x_i) + \frac{\phi(p_3) - \phi(p_1)}{\Delta y}(y - y_j). \quad (31)$$

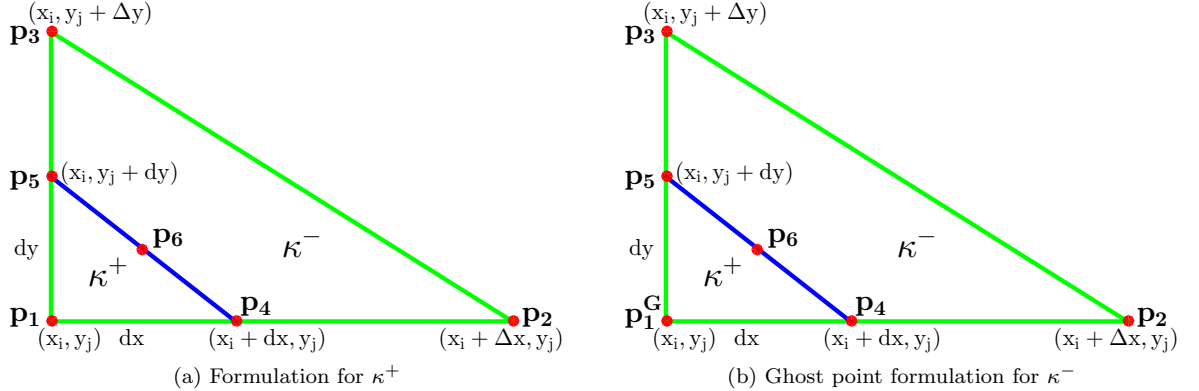


Figure 5: Case 1 - the interface cutting through two legs

For an interface cell, κ there are two cases. Case 1 is when the interface cuts through two legs of κ (as in Figure 5), and Case 2 is when the interface cuts through one leg and the hypotenuse of κ (as in Figure 6). As

an example, we construct the extension function for Case 1 and the construction for Case 2 follows similarly. Then for Case 1,

$$U^h(\phi^h) = \begin{cases} \phi(p_1) + \phi_x^+(x - x_i) + \phi_y^+(y - y_j) & \text{for } (x, y) \in \kappa^+, \\ \phi(p_2) + \phi_x^-(x - x_i - \Delta x) + \phi_y^-(y - y_j) & \text{for } (x, y) \in \kappa^-, \end{cases} \quad (32)$$

where for $(x, y) \in \kappa^+$ (as in Figure 5(a),),

$$\phi_x^+ = \frac{\phi(p_4) - \phi(p_1)}{dx} \quad \& \quad \phi_y^+ = \frac{\phi(p_5) - \phi(p_1)}{dy}, \quad (33)$$

and for $(x, y) \in \kappa^-$ (as in Figure 5(b)),

$$\phi_x^- = \frac{\phi(p_2) - \phi(p_4)}{\Delta x - dx} \quad \& \quad \phi_y^- = \frac{\phi(p_3) - \phi(p_5)}{\Delta y - dy}. \quad (34)$$

Above it is assumed that the extensions of p_3p_5 and p_2p_4 intersect at a ghost point, p_1^G and hence

$$\frac{\phi(p_1^G) - \phi(p_4)}{dx} = \frac{\phi(p_4) - \phi(p_2)}{\Delta x - dx} \quad \& \quad \frac{\phi(p_1^G) - \phi(p_5)}{dy} = \frac{\phi(p_1^G) - \phi(p_3)}{\Delta y}. \quad (35)$$

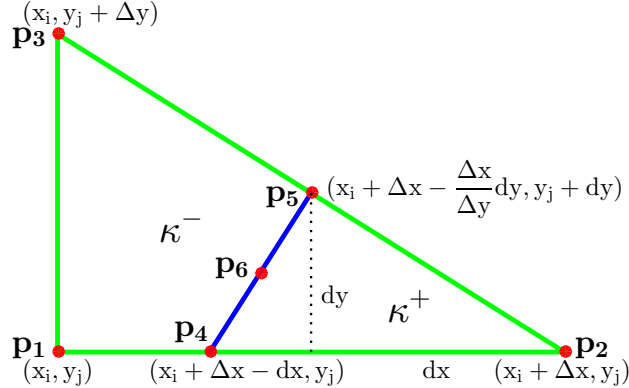


Figure 6: Case 2 - the interface cutting through one leg and the hypotenuse

We note that ϕ_x^+ and ϕ_x^- are linear functions of $\phi(p_1), \phi(p_2), \phi(p_3)$ and $\phi(p_4)$ from eq. (33) and eq. (34). We rewrite eq. (35) as

$$\phi(p_5) = \phi(p_1^G) - \frac{dy}{\Delta y} (\phi(p_1^G) - \phi(p_3)) \quad (36)$$

$$\phi(p_1^G) = \phi(p_4) + \frac{dx}{\Delta x - dx} (\phi(p_4) - \phi(p_2)) \quad (37)$$

Using eq. (36) and eq. (37) in eq. (33) and eq. (34), ϕ_y^+ and ϕ_y^- respectively can be obtained as linear functions of $\phi(p_1), \phi(p_2), \phi(p_3)$ and $\phi(p_4)$. The kinematic condition, eq. (29), is imposed as given below,

$$0 = \mathbf{K}^+ \lambda^+ \nabla \phi^+ \cdot \hat{\mathbf{n}} - \mathbf{K}^- \lambda^- \nabla \phi^- \cdot \hat{\mathbf{n}}. \quad (38)$$

Given $\hat{\mathbf{n}} = (n_1, n_2) = \left(\frac{-dy}{\sqrt{dx^2 + dy^2}}, \frac{-dx}{\sqrt{dx^2 + dy^2}} \right)$ and the permeability $\mathbf{K} = \begin{pmatrix} k & 0 \\ 0 & k \end{pmatrix}$ for an isotropic porous medium, eq. (38) reduces to

$$k^+ \lambda^+ \phi_x^+ n_1 + k^+ \lambda^+ \phi_y^+ n_2 = k^- \lambda^- \phi_x^- n_1 + k^- \lambda^- \phi_y^- n_2. \quad (39)$$

Using eq. (39), $\phi(p_4)$ is eliminated so that, ϕ_x^+ , ϕ_y^+ , ϕ_x^- and ϕ_y^- are obtained uniquely as linear combinations of $\phi(p_1)$, $\phi(p_2)$ and $\phi(p_3)$ in such a way that the coefficients are finite and independent of ϕ^h . Thus the extension operator U^h , given by eq. (32), for Case 1 of an interface cell becomes well defined as in the case of a regular cell given by eq. (31). Similarly, $U^h(\phi^h)$ can be defined for Case 2 of an interface cell (Figure 6) with finite and well defined coefficients in the following way,

$$U^h(\phi^h) = \begin{cases} \phi(p_2) + \phi_x^+(x - x_i - \Delta x) + \phi_y^+(y - y_j) & \text{for } (x, y) \in \kappa^+, \\ \phi(p_1) + \phi_x^-(x - x_i) + \frac{\phi(p_3) - \phi(p_1)}{\Delta y}(y - y_j) & \text{for } (x, y) \in \kappa^-. \end{cases} \quad (40)$$

where

$$\phi_x^+ = \frac{\phi(p_2) - \phi(p_4)}{dx} \quad \& \quad \phi_y^+ = \frac{\phi(p_5) - \phi(p_2)}{dy} + \frac{\phi(p_2) - \phi(p_4)}{dx} \frac{\Delta x}{\Delta y} \quad (41)$$

$$\phi_x^- = \frac{\phi(p_4) - \phi(p_1)}{\Delta x - dx} \quad (42)$$

Using the extension functions as defined above, the weak formulation eq. (30) reduces to finding a discrete function $\phi^h \in H^{1,h}$ such that it satisfies Eq. (28b) on the boundary points and so that for all $\psi^h \in H^{1,h}$,

$$\begin{aligned} \sum_{K \in L^h} \left(\int_{K^+} \mathbf{K}\lambda \nabla U^h(\phi^h) \nabla U^h(\psi^h) + \int_{K^-} \mathbf{K}\lambda \nabla U^h(\phi^h) \nabla U^h(\psi^h) - \int_{\partial K} \mathbf{K}\lambda U^h(\psi^h) \nabla U^h(\phi^h) \cdot \hat{\mathbf{n}} \right) \\ = \sum_{K \in L^h} \left(\int_{K^+} f U^h(\psi^h) + \int_{K^-} f U^h(\psi^h) \right). \end{aligned} \quad (43)$$

It can be shown that if $\mathbf{K}(\mathbf{x})$ is positive definite, then the matrix obtained for the linear system of the discretized weak form, eq. (43), is also positive definite and is therefore invertible.

3.2.1 Polymer flood

The transport equations, eq. (16b) and eq. (16c), are solved using a Modified version of the Method Of Characteristics (MMOC). At first we rewrite eqs. (16b) and (16c) in a non-conservative form as follows

$$\phi s_t + \frac{\partial f}{\partial s} \mathbf{v} \cdot \nabla s + \nabla \cdot (D \nabla s) = g_1 - \frac{\partial f}{\partial c} \mathbf{v} \cdot \nabla c \quad (44a)$$

$$\phi c_t + \left(\frac{f}{s} \mathbf{v} + \frac{D}{s} \nabla s \right) \cdot \nabla c + c \frac{g_1}{s} = \frac{g_2}{s} \quad (44b)$$

where $D(s, c) = \mathbf{K}(\mathbf{x})\lambda_o(s)f(s, c)\frac{dp_c(s)}{ds}$, $g_1 = q_a$ and $g_2 = c_{inj}q_a$. In eq. (44a) we replace the transport operator, $\phi s_t + \frac{\partial f}{\partial s} \mathbf{v} \cdot \nabla s$ by a derivative along its characteristic direction in the following way

$$\frac{\partial}{\partial \tau_s} = \frac{1}{\psi_s} \left(\phi \frac{\partial}{\partial t} + \frac{\partial f}{\partial s} \mathbf{v} \cdot \nabla \right) \quad (45)$$

where τ_s is used to parametrize the characteristics and ψ_s is a suitable normalization that simplifies the numerical discretization of the characteristic derivative and is defined by

$$\psi_s = \left[\phi^2 + \left(\frac{\partial f}{\partial s} \right)^2 |\mathbf{v}|^2 \right]^{1/2} \quad (46)$$

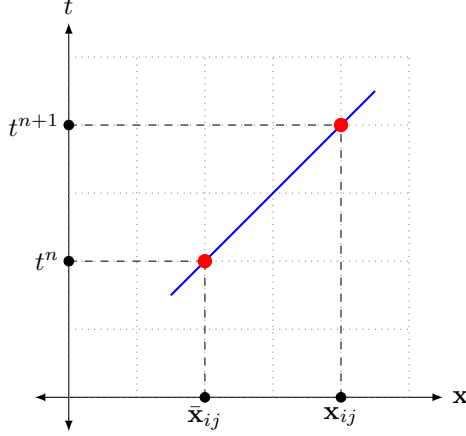


Figure 7: Discrete approximation of the characteristic curve from $\bar{\mathbf{x}}_{ij}$ to \mathbf{x}_{ij} in 1D

Then eq. (44a) is equivalently written in the form

$$\psi_s \frac{\partial s}{\partial \tau_s} + \nabla \cdot (D \nabla s) = g_1 - \frac{\partial f}{\partial c} \mathbf{v} \cdot \nabla c \quad (47)$$

For numerical computation, we use the spatial grid described in § 3.1 and the time interval $[0, T]$ is uniformly divided into N subintervals of length Δt , such that $t^n = n\Delta t$ and $T = N\Delta t$. Then we denote the grid values of the variables by $w_{ij}^n = w(\mathbf{x}_{ij}, t^n)$ where $\mathbf{x}_{ij} = \mathbf{x}(ih, jh)$. Consider that the solution is known at some time t^n and the solution at a subsequent time t^{n+1} needs to be computed. Then starting from any point $(\mathbf{x}_{ij}, t^{n+1})$ we trace backward along the characteristics to a point $(\bar{\mathbf{x}}_{ij}, t^n)$ where the solution is already known. Let the characteristics which originate from the point $\bar{\mathbf{x}}_{ij}$ at time t^n reach the point \mathbf{x}_{ij} at time t^{n+1} (see Figure 7). From the equation of the characteristic curves given by

$$\frac{d\mathbf{x}}{d\tau_s} = \frac{1}{\phi} \frac{\partial f}{\partial s} \mathbf{v}$$

we can use numerical discretization to obtain an approximate value of $\bar{\mathbf{x}}_{ij}$ in the following way

$$\bar{\mathbf{x}}_{ij} = \mathbf{x}_{ij} - \frac{\partial f}{\partial s} (s_{ij}^n, c_{ij}^n) \mathbf{v}_{ij}^n \Delta t / \phi.$$

Using the above equation, the derivative in the characteristic direction, defined by eq. (45), is approximated by:

$$\psi_s \frac{\partial s}{\partial \tau_s} \approx \psi_s \frac{s(\mathbf{x}_{ij}, t^{n+1}) - s(\bar{\mathbf{x}}_{ij}, t^n)}{[(\mathbf{x}_{ij} - \bar{\mathbf{x}}_{ij})^2 + (\Delta t)^2]^{1/2}} = \phi \frac{s_{ij}^{n+1} - \bar{s}_{ij}^n}{\Delta t}$$

This leads to the following implicit-time finite difference formulation for eq. (47)

$$\phi \frac{s_{ij}^{n+1} - \bar{s}_{ij}^n}{\Delta t} + \nabla_h (\bar{D} \nabla_h s)_{ij}^{n+1} = (g_1)_{ij} - \left(\frac{\partial f}{\partial c} \right)_{ij}^n (\mathbf{v}_{ij}^n \cdot \nabla_h c_{ij}^n) \quad (48)$$

where

$$\begin{aligned}\bar{s}_{ij}^n &= s(\bar{\mathbf{x}}_{ij}, t^n) \quad \& \quad \bar{D}_{ij}^n = D(\bar{s}_{ij}^n, c_{ij}^n) \\ \boldsymbol{\nabla}_h (\bar{D} \boldsymbol{\nabla}_h s)_{ij}^{n+1} &= \bar{D}_{i+1/2,j} \frac{s_{i+1,j}^{n+1} - s_{i,j}^{n+1}}{\Delta x^2} - \bar{D}_{i-1/2,j} \frac{s_{i,j}^{n+1} - s_{i-1,j}^{n+1}}{\Delta x^2} \\ &\quad + \bar{D}_{i,j+1/2} \frac{s_{i,j+1}^{n+1} - s_{i,j}^{n+1}}{\Delta y^2} - \bar{D}_{i,j-1/2} \frac{s_{i,j}^{n+1} - s_{i,j-1}^{n+1}}{\Delta y^2} \\ \bar{D}_{i\pm 1/2,j} &= \frac{D(\bar{s}_{i\pm 1,j}^n, c_{i\pm 1,j}^n) + D(\bar{s}_{i,j}^n, c_{i,j}^n)}{2} \\ \bar{D}_{i,j\pm 1/2} &= \frac{D(\bar{s}_{i,j\pm 1}^n, c_{i,j\pm 1}^n) + D(\bar{s}_{i,j}^n, c_{i,j}^n)}{2}\end{aligned}$$

Following the same procedure as before we define the following equations, analogous to eq. (45), eq. (46) and eq. (47), for the concentration equation eq. (44b)

$$\begin{aligned}\psi_c &= \left[\phi^2 + \left(\frac{f}{s} \right)^2 |\mathbf{v}|^2 + \left(\frac{\bar{D}}{s} \right)^2 |\boldsymbol{\nabla} s|^2 \right]^{1/2} \\ \frac{\partial}{\partial \tau_c} &= \frac{1}{\psi_c} \left(\phi \frac{\partial}{\partial t} + \frac{f}{s} \mathbf{v} \cdot \boldsymbol{\nabla} + \frac{\bar{D}}{s} \boldsymbol{\nabla} s \cdot \boldsymbol{\nabla} \right)\end{aligned}$$

Then using the updated saturation values, the derivative in the characteristic direction, τ_c of the operator $\phi c_t + \frac{f}{s} \mathbf{v} \cdot \boldsymbol{\nabla} s + \frac{\bar{D}}{s} \boldsymbol{\nabla} s \cdot \boldsymbol{\nabla} c$ is approximated using the following:

$$\bar{\mathbf{x}}_{ij}^c = \mathbf{x}_{ij}^c - \left(\left(\frac{f}{s} \right) (s_{ij}^n, c_{ij}^n) \mathbf{v} + \left(\frac{D}{s} \right) (\bar{s}_{ij}^n, c_{ij}^n) \boldsymbol{\nabla} s \right) \Delta t / \phi,$$

where, as before, $\bar{\mathbf{x}}_{ij}^c$ is the origin point of the characteristics which reach \mathbf{x}_{ij}^c at time t^{n+1} . Thus we arrive at the following implicit-time finite difference formulation for Eq. (44b)

$$\phi \frac{c_{ij}^{n+1} - \bar{c}_{ij}^n}{\Delta t} + \frac{(g_1)_{ij}}{s_{ij}^n} c_{ij}^{n+1} = \frac{(g_2)_{ij}}{s_{ij}^n} \quad (49)$$

where $\bar{c}_{ij}^n = c(\bar{\mathbf{x}}_{ij}^c, t^n)$. Hence Eq. (48) and Eq. (49) form the finite difference approximation of the transport equations, Eq. (44a) and Eq. (44b) respectively.

3.2.2 Surfactant-polymer flood

The problem set up is similar to the polymer flooding case, with a few modifications. The computations are done on the same grid set up for both the pressure equation and the surfactant equations. The finite element method for the pressure equation, eq. (22a), is also implemented in the same way while the treatment of the transport equations, eq. (22b) - eq. (22d), using the method of characteristics is described in detail below. For the purpose of solving these transport equations using MMOC, it is useful to define the following:

$$\begin{aligned}\mathbf{b}_s &= \frac{\partial f}{\partial s} \mathbf{v}, & \psi_s &= \left(\phi^2 + |\mathbf{b}_s|^2 \right)^{1/2}, \\ \mathbf{b}_c &= \frac{f}{s} \mathbf{v} + \frac{\tilde{D}}{s} \frac{\partial p_c}{\partial s} \boldsymbol{\nabla} s + \frac{\tilde{D}}{s} \frac{\partial p_c}{\partial \Gamma} \boldsymbol{\nabla} \Gamma, & \psi_c &= \left(\phi^2 + |\mathbf{b}_c|^2 \right)^{1/2}, \\ \mathbf{b}_\Gamma &= \frac{f}{s} \mathbf{v} + \frac{\tilde{D}}{s} \frac{\partial p_c}{\partial s} \boldsymbol{\nabla} s + \frac{\tilde{D}}{s} \frac{\partial p_c}{\partial \Gamma} \boldsymbol{\nabla} \Gamma, & \psi_\Gamma &= \left(\phi^2 + |\mathbf{b}_\Gamma|^2 \right)^{1/2}.\end{aligned}\quad (50)$$

Also let the characteristic parameters, τ_s , τ_c and τ_Γ respectively be associated with the operators $\phi s_t + \mathbf{b}_s \cdot \nabla s$, $\phi c_t + \mathbf{b}_c \cdot \nabla c$ and $\phi \Gamma_t + \mathbf{b}_\Gamma \cdot \nabla \Gamma$ and the derivatives are given by,

$$\begin{aligned}\frac{\partial}{\partial \tau_s} &= \frac{\phi}{\psi_s} \frac{\partial}{\partial t} + \frac{1}{\psi_s} \mathbf{b}_s \cdot \nabla, \\ \frac{\partial}{\partial \tau_c} &= \frac{\phi}{\psi_c} \frac{\partial}{\partial t} + \frac{1}{\psi_c} \mathbf{b}_c \cdot \nabla, \\ \frac{\partial}{\partial \tau_\Gamma} &= \frac{\phi}{\psi_\Gamma} \frac{\partial}{\partial t} + \frac{1}{\psi_\Gamma} \mathbf{b}_\Gamma \cdot \nabla.\end{aligned}\quad (51)$$

Then using eq. (50) and eq. (51), the transport equations, eq. (22b) - eq. (22d) are rewritten as

$$\begin{aligned}\psi_s \frac{\partial s}{\partial \tau_s} + \nabla \cdot \left(\tilde{D} \frac{\partial p_c}{\partial s} \nabla s \right) &= g_1 - \frac{\partial f}{\partial c} \mathbf{v} \cdot \nabla c - \frac{\partial f}{\partial \Gamma} \mathbf{v} \cdot \nabla \Gamma - \nabla \cdot \left(\tilde{D} \frac{\partial p_c}{\partial \Gamma} \nabla \Gamma \right), \\ \psi_c \frac{\partial c}{\partial \tau_c} + \frac{c}{s} g_1 &= \frac{1}{s} g_2, \\ \psi_\Gamma \frac{\partial \Gamma}{\partial \tau_\Gamma} + \frac{\Gamma}{s} g_1 &= \frac{1}{s} g_3.\end{aligned}\quad (52)$$

The characteristic derivative associated with parameter τ_s is computed by backward differencing along the τ_s -characteristic at (\mathbf{x}, t^{n+1}) , so that,

$$\tilde{\mathbf{x}}^{n+1} = \mathbf{x} - \frac{\mathbf{b}_s}{\phi} \Delta t^{n+1} \quad (53)$$

Then we see that

$$\psi_s \frac{\partial s}{\partial \tau_s} \approx \psi_s \frac{s(\mathbf{x}, t^{n+1}) - s(\mathbf{x}, t^{n+1} - \Delta t^{n+1})}{[(\mathbf{x} - \tilde{\mathbf{x}})^2 + (\Delta t^{n+1})^2]^{1/2}} = \phi \frac{s(\mathbf{x}, t^{n+1}) - s(\tilde{\mathbf{x}}, t^{n+1} - \Delta t^{n+1})}{\Delta t^{n+1}}, \quad (54)$$

where $s(\tilde{\mathbf{x}}, t^n)$ is evaluated via bilinear interpolation of the approximate solution values at the nearby grid points, at time level $t^n = n\Delta t$. Note that in Eq. (53) \mathbf{b}_s is evaluated approximately as $\left(\frac{\partial f}{\partial s} \mathbf{v} \right)^n$. The derivative associated with the characteristic directions τ_c and τ_Γ are obtained similarly. All of these lead to a system of implicit-time finite difference formulations, similar to eqs. (48) and (49) for the saturation eqs. (22b)–(22d).

3.3 Heterogeneity

In this paper, we use scalar, log-normal absolute permeability fields, $K(\mathbf{x})$ as a model for multi-scale rock heterogeneity in some of the numerical simulations of SP flooding. First we generate a Gaussian random field, $\xi(\mathbf{x})$ which we assume to be stationary(translational invariance of covariance function), isotropic(rotational invariance of covariance function) and fractal(self-similar). Hence, the distribution is characterized by a zero mean and a covariance function of the form:

$$cov(\xi(\mathbf{x}_1), \xi(\mathbf{x}_2)) = c |\mathbf{x}_1 - \mathbf{x}_2|^{-\beta}, \quad 0 < \beta < \infty \quad (55)$$

The scaling exponent β , called the Hurst coefficient, controls the nature of heterogeneity. With an increase in β the covariance function decays faster and hence heterogeneities in the shorter length scales become pronounced. The LABTRAN-GEO methods, [Borges et al., 2010] are computationally efficient methods to generate Gaussian fields with a covariance function given by the power law, Eq. (55). From this multi-scale Gaussian field, we construct an absolute permeability field and a porosity field as

$$K(\mathbf{x}) = k_0 \exp(\varpi \xi(\mathbf{x})), \quad (56)$$

$$\phi(\mathbf{x}) = \phi_0 + \bar{\varphi} \xi(\mathbf{x}), \quad \bar{\varphi} > 0 \quad (57)$$

where k_0 is a chosen threshold, $0 < \varpi \leq 1$ is a chosen scaling exponent and $\bar{\varphi}$ is a normalizing factor that is chosen to ensure that the porosity lies in the following range, $0.05 \leq \phi(\mathbf{x}) \leq 0.35$. The mean $\langle \mathbf{K} \rangle$ and variance σ_k^2 of the log-normal field \mathbf{K} are set by the coefficients k_0 and ϖ . With change in ϖ we get different values for the Coefficient of Variation CV for permeability (CV_k) and porosity (CV_ϕ). For the permeability field \mathbf{K} , this is defined by

$$CV_k = \frac{\sigma_k}{\langle \mathbf{K} \rangle}.$$

This dimensionless number CV can be thought of as a measure of the heterogeneity of the field. Similar formulations have been adopted in [Glimm et al., 1993, Furtado and Pereira, 2003, Abreu, 2014]. In Figure 8 we present an example of such a stationary, isotropic and multiscale Gaussian field calculated with zero mean, $\beta = 0.5$ and $c = 1/(1 - 2^{-\beta})$. It is to be noted that in our current simulations, variable porosity fields are not used. But we present the method for generating such fields for future use.

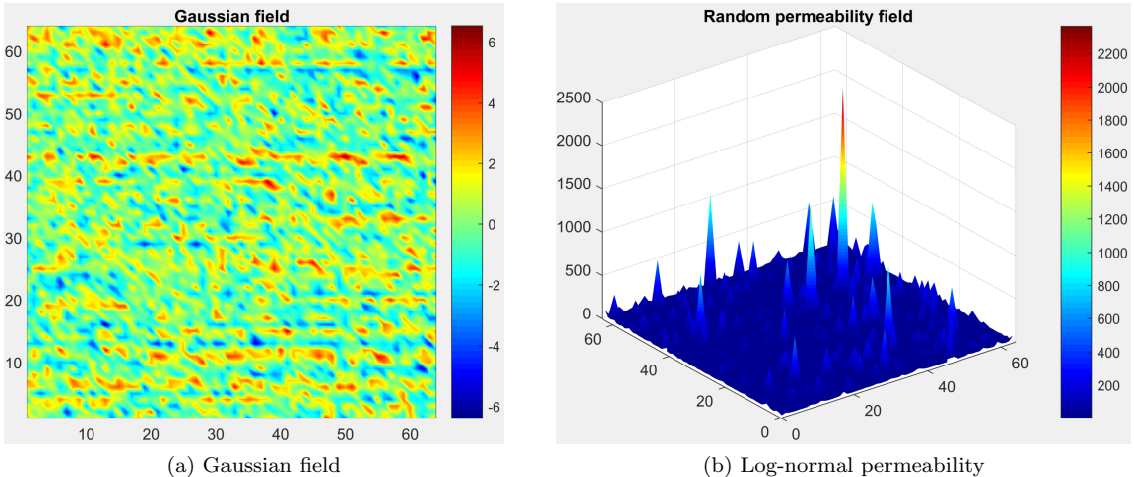


Figure 8: Stationary, isotropic, fractal Gaussian field, $\xi(\mathbf{x})$ [shown in (a)] used for generating a log-normal permeability, $\mathbf{K}(\mathbf{x})$ [shown in (b)] using eq. (56). Both fields are of size 64×64 .

3.4 Algorithm

Here we give a detailed algorithm for the SP flood simulation. The algorithm for the polymer flood is essentially a special case of the same. The step-by-step algorithm is given as follows:

1. Define the Cartesian grid in the domain using equal, uniform grid sizes in both the axes. Generate the finite element mesh.
2. Generate a heterogeneity field on this grid.
3. Choose an initial interface separating the injected fluid from the resident fluid.
4. Set the model parameters: μ_o , μ_w , $s_{ro}^{\sigma 0}$, $s_{ra}^{\sigma 0}$.
5. Initialize the state variables s , c and Γ as

$$s_0 = \begin{cases} 1 & x \in \Omega^+ \\ s_0^{\sigma 0} & x \in \Omega^- \end{cases}, \quad c_0 = \begin{cases} 0.05 & x \in \Omega^+ \\ 0 & x \in \Omega^- \end{cases}, \quad \Gamma_0 = \begin{cases} 0.005 & x \in \Omega^+ \\ 0 & x \in \Omega^- \end{cases}.$$

6. Calculate $\sigma(s^n, \Gamma^n)$, $\mu_a(c^n)$, $s_{ra}(s^n, \Gamma^n)$, $s_{ro}(s^n, \Gamma^n)$, $\lambda_a(s^n, c^n, \Gamma^n)$, $\lambda_o(s^n, c^n, \Gamma^n)$, $\lambda(s^n, c^n, \Gamma^n)$ using s^n , c^n , Γ^n which are values of s , c and Γ respectively at the n^{th} time level.
7. Solve the global pressure equation to get p^n and subsequently compute v^n .
8. Use v^n , s^n , c^n , Γ^n and the quantities calculated in Step 6, to solve for s^{n+1} , c^{n+1} and Γ^{n+1} , thus completing a full time step.
9. If breakthrough is achieved: then stop; else update $n = n + 1$ and Repeat from Step 6.

In order to improve speed, sometimes a few iterations of Steps 6 and 8 are done before updating the pressure in Step 7. The pseudocode (see Algorithm 1) and flow-chart (see Figure 9) for the procedure are given here.

Algorithm 1: SP flooding simulation

```

/* Set up Cartesian grid, FE Mesh, permeability field and model parameters */

1 Set  $i, j = 0, \dots, M$ ;  $\mathbf{x}_{ij} = \left( \frac{i}{M}, \frac{j}{M} \right)$ ; /* ( $M \times M$  is the grid size) */
2 Set  $\Sigma = \text{Initial interface}$ ; /*  $\Sigma = \partial\Omega^+ \cap \partial\Omega^-$  */
3 Set  $\mathbf{K}(\mathbf{x}) = \text{block inclusion or SPE10 or log-normal}$  ;
4 Set  $\mu_o, \mu_w, s_{ro}^{\sigma 0}, s_{ra}^{\sigma 0}, \tilde{q} = \text{values from Table 1}$ ;

/* Initialization */

5 Set  $t = 0$ ;  $\Delta t = \frac{1}{N}$ ;  $Tstop = N\Delta t$ ; /*  $N$  chosen for accuracy */
6 for  $i = 0, \dots, M$  do
7   for  $j = 0, \dots, M$  do
8     Set  $(s, c, \Gamma)(\mathbf{x}_{ij}, 0) = \begin{cases} (1, 0, 0) & \mathbf{x}_{ij} \in \Omega^+ \\ (s_0^{\sigma 0}, c_0, \Gamma_0) & \mathbf{x}_{ij} \in \Omega^- \end{cases}$ ;
9   end
10 end

/* Computation loop */

11 while  $(s(\mathbf{x}_{M,M}, t) \leq 1 - s_0^{\sigma 0} \ \&\ t < Tstop)$  do
12   Compute  $\{\sigma, \mu_a, s_{ra}, s_{ro}, \lambda_a, \lambda_o, \lambda, p_c\}$  using  $(s^n, c^n, \Gamma^n, \mathbf{v}^{n-1})$ ;
13   Solve global pressure equation for  $p^n, v^n$ ;
14   Recompute  $\{s_{ra}, s_{ro}, \lambda_a, \lambda_o, \lambda\}$  using  $(s^n, c^n, \Gamma^n, \mathbf{v}^n)$ ;
15   Solve transport equations for  $s^{n+1}$ ,  $c^{n+1}$  and  $\Gamma^{n+1}$ ;
16   Set  $t = t + \Delta t$ ;
17 end

```

4 Results and discussion

The numerical simulations have been carried out on a square domain, $\Omega = [0, 1]^2$ which represents a quarter five-spot design and on a variety of different grid sizes. The first set of simulations is designed to qualitatively validate the method against some known results in the literature. The rest of the simulations is aimed at exploring and identifying favorable aspects of more complex surfactant-polymer flooding strategies. These simulations have been performed on a variety of homogeneous and heterogeneous spatial permeability field data that have been either generated numerically or imported from the SPE10 benchmark problem and with input parameters listed in Table 1.

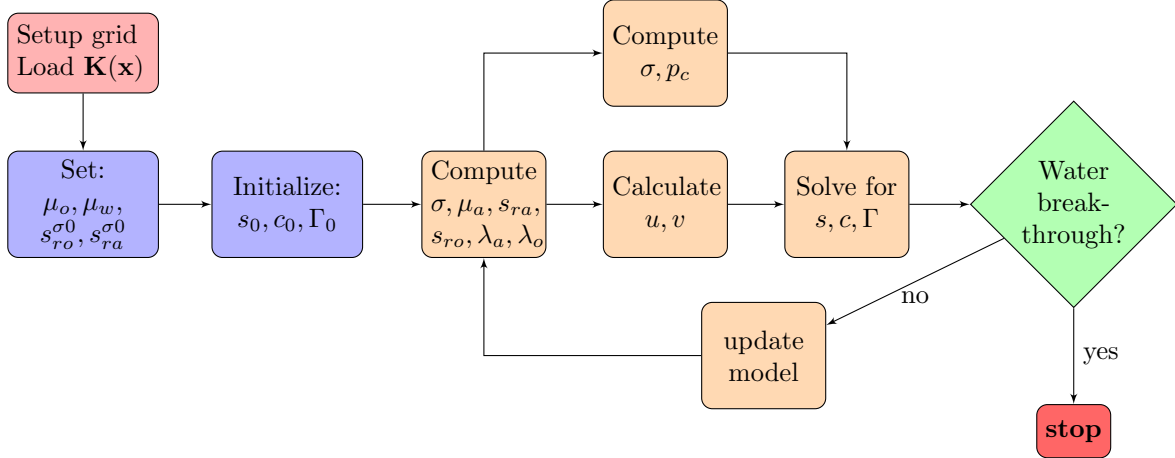


Figure 9: Flow-chart for SP flooding simulation

Table 1: Simulation input data

Model parameter	Symbol	Value
Spatial grid size	$h \times k$	variable
Porosity	ϕ	1
Permeability	\mathbf{K}	variable
Initial resident water saturation	$s_0^{\sigma 0}$	0.21
Polymer injection concentration	c_0	variable
Surfactant injection concentration	Γ_0	variable
Oil viscosity	μ_o	12.6
Pure water viscosity	μ_w	1.26
Residual aqueous phase saturation	s_{ra}	0.1
Residual oleic phase saturation	s_{ro}	0.3
Critical capillary number of aqueous phase	N_{cao}	10^{-5}
Critical capillary number of oleic phase	N_{co}	10^{-5}
Parameters of capillary pressure relation [eq. (23)]	ω_1, ω_2	0.1, 0.4
Injection rate	\tilde{q}	200
Time step size	Δt	1/25

4.1 Numerical validation

Waterflooding with one block inclusion in permeability

For validation, we first consider a special case of a porous medium that has a square inclusion with lower permeability. We set the permeability of the shaded block (Figure 10) to be 1000 times smaller than in the rest of the domain. We simulate the displacement of resident oil with a waterflood using a 30×30 grid on a quarter five-spot domain, Ω . The water saturation contours inside the domain are compared at four different time points during the displacement process (Figure 11). We observe that the numerical method captures the region of discontinuity of the permeability very well and the results are in qualitative agreement with similar simulation studies found in the literature (see [Li and Rivière, 2014]).

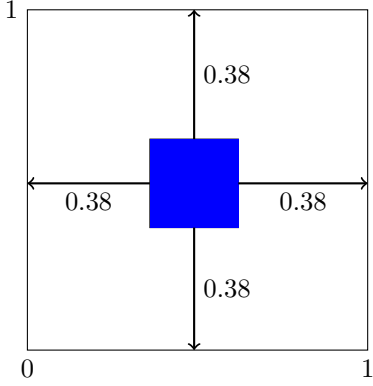


Figure 10: Piecewise continuous permeability field with one square inclusion

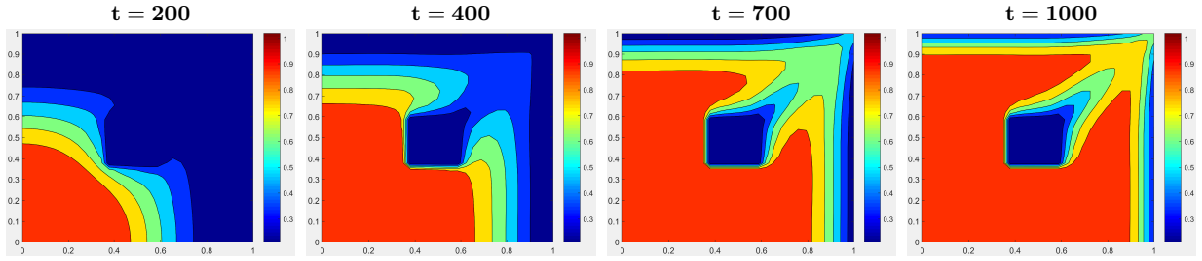


Figure 11: Saturation contours during a waterflood in a quarter five-spot reservoir with a spatial resolution of 30×30 . The permeability field is piecewise continuous with a block inclusion at the center. The contours are plotted at four different time levels, t .

Waterflooding with two block inclusions in permeability

In the second validation experiment, we consider a permeability field with two rectangular inclusions inside the domain. As before, the permeability of the shaded blocks (Figure 12) is set to be 1000 times smaller than in the rest of the domain. A waterflood is simulated on a 30×30 grid and the water saturation contours inside the domain at different points of time during the flooding process are compared (Figure 13). We observe that the numerical method is successful in qualitatively capturing the discontinuity in the permeability data very well and the saturation contours appear to be in good qualitative agreement with what is expected based on physics.

Waterflooding the Upper-Ness (SPE10) permeability field

In this simulation we use a 30×30 block of permeability field data from the Upper-Ness region of the SPE10 benchmark problem dataset (see [Christie and Blunt, 2001]). The original dataset is described on a regular Cartesian grid with $60 \times 220 \times 85$ (1,122,000) cells. The model consists of two types of formations: a shallow-marine Tarbert formation in the top 35 layers with relatively smooth permeability, and a fluvial Upper-Ness permeability in the bottom 50 layers. Both formations (Figure 14) are characterised by large permeability variations (8 to 12 orders of magnitude), but are different qualitatively. The Upper-Ness formation is somewhat more challenging than the Tarbert formation because not only does it contain the intricate variations in permeability, the range of variations is also larger. Here we only present the results obtained using the permeability field data from the Upper-Ness formation (Figure 14(a)).

As expected, the highly heterogeneous rock matrix leads to development of undesirable finger formations while the high viscosity ratio ($M = \mu_o/\mu_w = 10$) between the displaced and displacing phase leads to the

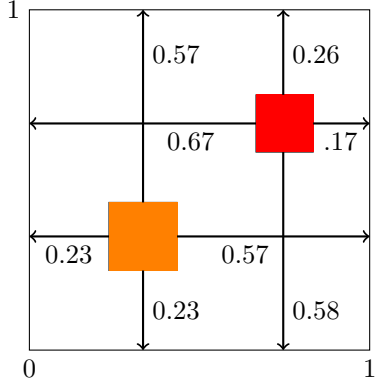


Figure 12: Piecewise continuous permeability field with two square inclusions

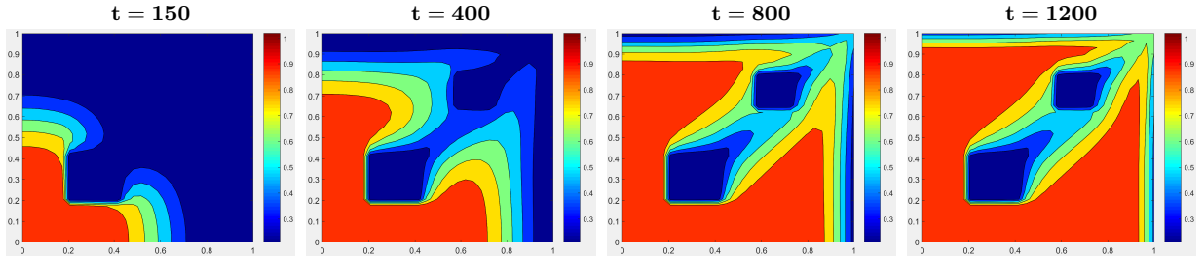


Figure 13: Saturation contours during a waterflood in a quarter five-spot reservoir with a spatial resolution of 30×30 . The permeability field is piecewise continuous with two block inclusions as shown in Figure 12. The contours are plotted at four different time levels.

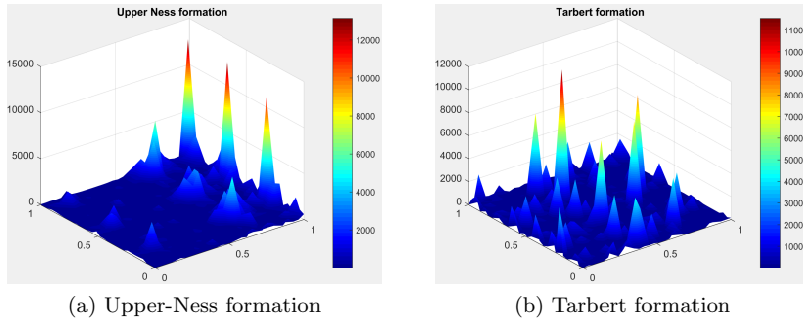


Figure 14: Permeability plots from the SPE10 benchmark dataset.

growth of these viscous fingers. We observe that the displacing phase progresses towards the production well (located at $(x, y) = (1, 1)$) by sweeping through the regions of higher permeability values. The method captures the expected features of fluid flow through the regions of high and low permeability very well and the fronts are well resolved. This provides qualitative validation of the model and the numerical method as it is able to capture the expected physical phenomenon like viscous finger formations in fully developed flows.

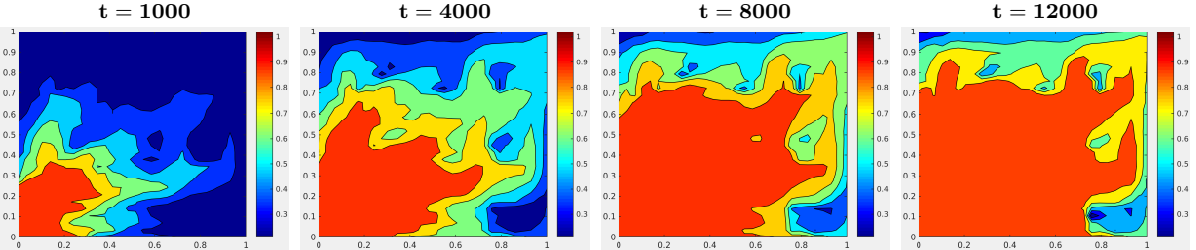


Figure 15: Saturation contours during a waterflood in a quarter five-spot reservoir with 30×30 spatial resolution. The permeability field is of Upper-Ness formation type (see Figure 14(a)). The contours are plotted at four different time levels.

4.2 Polymer flood simulations

The displacement processes involved in tertiary oil recovery methods like polymer flooding and surfactant-polymer flooding are usually unstable to begin with. Hence one of the fundamental fluid dynamical mechanisms that is employed to improve oil recovery is to delay and slow down the development of these instabilities that lead to fingers since there is always a finite reservoir area that needs to be swept. It is understood that the nonlinear fingers evolve from infinitesimal interfacial hydrodynamic disturbances at early stages of the flow. The growth of these initial disturbances can be controlled by choosing optimal viscous profiles for the injection fluid i.e. by choosing optimal values of the viscosity ratio [Daripa and Pasa, 2004], among other things. The following set of simulations have been performed to compare the flow characteristics of a waterflood with that of a polymer flood.

Polymer flooding the Upper-Ness permeability field

In this simulation, we again use the Upper-Ness permeability field data on a 30×30 grid. We compare the flow patterns of a water flood ($c_0 = 0$) with that of a polymer flood where the concentration of polymer in the injected phase is $c_0 = 0.1$. The change in viscosity ratio from $M = \mu_o/\mu_w = 10$ in the water flood to $M = \mu_o/\mu_w = 1.7$ in the polymer flood gives rise to a marked change in the sweeping efficiency of the process. The comparison between water saturation contours of the water flood and the polymer flood is given in Figure 16. The figures clearly confirm the improved sweeping efficiency of the polymer flood process.

Grid refinement study with polymer flooding

In the next simulation of polymer flooding, we refine the grid over three steps - 15×15 , 30×30 and 60×60 . The domain is chosen to be a quarter of a five-spot pattern with two rectangular inclusions in the permeability field such that the permeability of the shaded blocks (Figure 12) is 1000 times smaller than in the rest of the domain. The injection concentration of the polymer in the aqueous solution is kept fixed at $c_0 = 0.1$ (viscosity ratio, $M = 1.67$). The water saturation contours for the polymer flooding process with three different grid sizes are given in Figure 17. We observe that even over the wide range of grid sizes the evolution of the fronts near the region of discontinuous permeability is captured effectively. The details in the high gradient region of the saturation contours become more prominent with the reduction in mesh size due to the additional computational points added to the domain. The qualitative agreement between the saturation contours at the same time levels but with different grid sizes provide further validation to the numerical convergence of the current method.

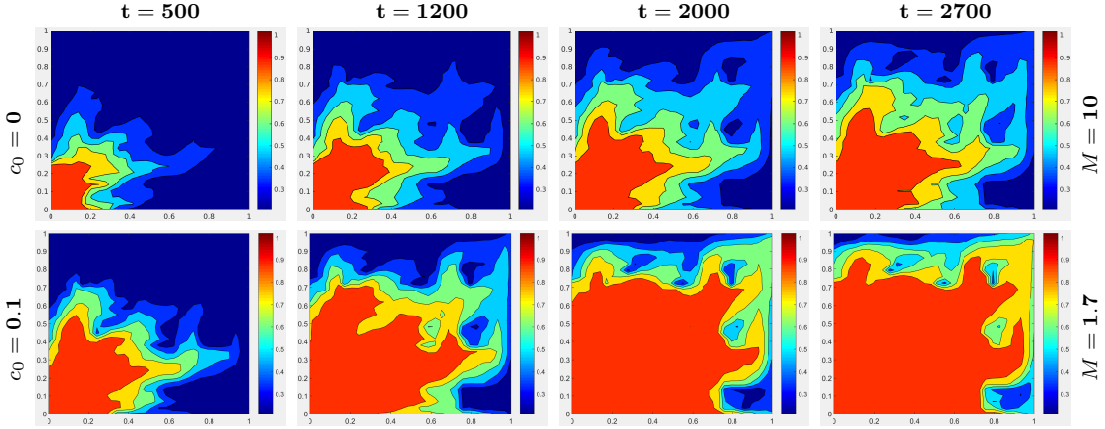


Figure 16: Saturation contours comparing a waterflood with a polymer flood in a quarter five-spot reservoir with spatial resolution of 30×30 . The contours are plotted at four different time levels. The simulations were carried out on the Upper-Ness formation type permeability field (see Figure 14(a)). The first row figures correspond to a waterflood ($c_0 = 0, M = 10$) and the second row corresponds to a polymer flood ($c_0 = 0.1, M = 1.7$) where c_0 is the polymer concentration in the injected aqueous phase and $M = \mu_o/\mu_a$ is the viscosity ratio of the resident oleic phase to the injected aqueous phase.

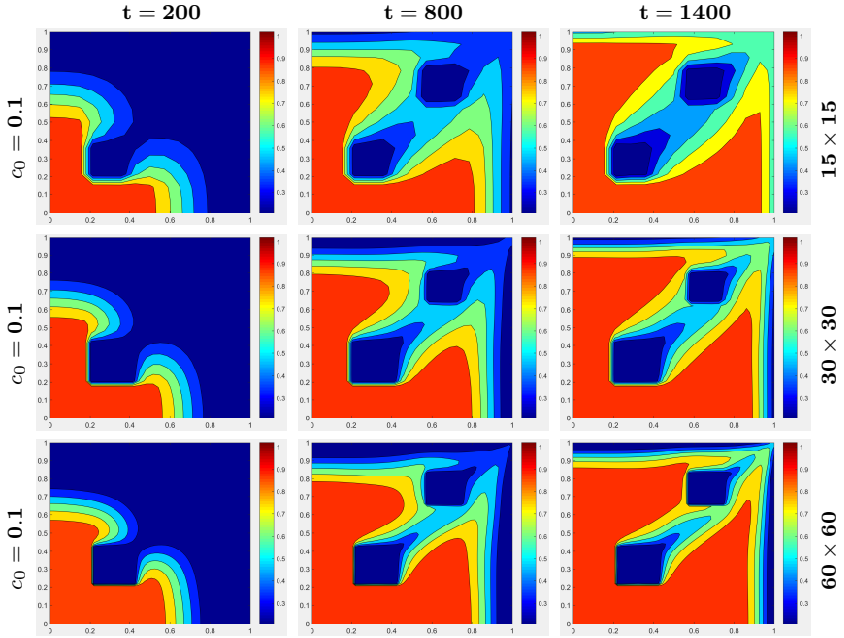


Figure 17: Water saturation contours during a polymer flood in a quarter five-spot reservoir with a piecewise continuous permeability field containing two block inclusions. The contours have been plotted at three different time levels. The simulations were performed on three different spatial resolutions : Row 1 - 15×15 , Row 2 - 30×30 and Row 3 - 60×60 .

4.3 Surfactant-polymer flood simulations

The final two sets of simulations are performed for surfactant-polymer flooding of a quarter five-spot reservoir fitted with a 24×24 grid. For all these simulations, a multi-scale, stationary, isotropic Gaussian permeability

field (Figure 18) generated using the method outlined in Section 3.3 has been used to construct a scalar, log-normal permeability field with $k_0 = 3.44253$, $\varpi = 1.0$ ($CV = 0.5$). The goals of these simulations are: (a) to demonstrate the robustness of the method in performing simulations of various different types of physical flooding processes and (b) to compare the effect of different concentrations of the injected polymer and the surfactant on improving the sweeping efficiency, controlling the growth of fingers and enhancing the overall oil recovery. These comparisons have only been exhibited qualitatively in this current work.

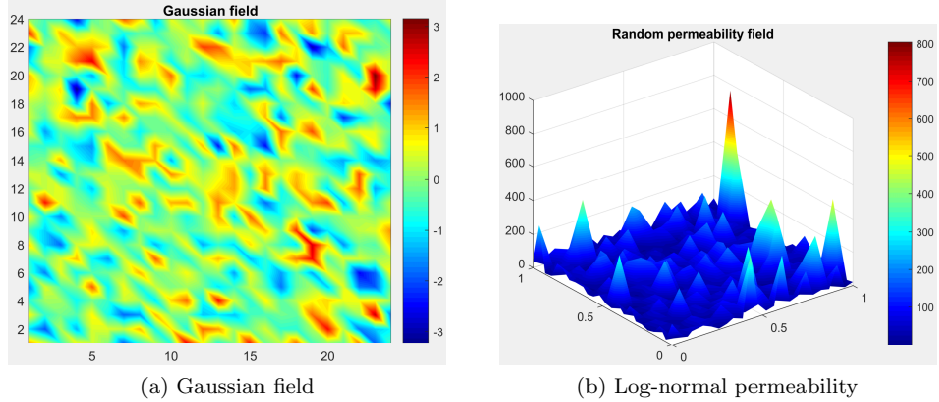


Figure 18: Multi-scale, stationary, isotropic Gaussian distribution [shown in (a)] which is used to generate a scalar log-normal permeability field [shown in (b)] of spatial resolution 24×24 .

The first set of simulations have been carried out by varying the concentration of the injected polymer in three steps ($c_0 = 0.01, 0.1$ and 0.3) and keeping the concentration of the injected surfactant fixed at $\Gamma_0 = 0.01$. The water saturation contours, polymer concentration contours and surfactant concentration contours at four different time levels of the flooding process have been presented in Figures 19–21 respectively. We observe that with an increase in the concentration of the injected polymer, there is a gradual smoothing out of the fingers in the water saturation, polymer and saturation concentration contours. This effect is more prominent in the high gradient region near the advancing “fronts” where the sharper details of the fingers become more rounded with an increase in the injected polymer concentration from 0.01 to 0.3 . It is to be noted that the effect is not as much pronounced as in the comparison between water flood and polymer flood simulations (Figure 16). This is because the change in viscosity ratios ($M = 1.25, 1.67, 1.96$) between the three different cases of surfactant-polymer flood simulations is not as high.

The second and final set of simulations have been carried out by varying the concentration of the injected surfactant in three steps ($\Gamma_0 = 0.001, 0.01$ and 0.1) and keeping the concentration of the injected polymer fixed at $c_0 = 0.1$ (the viscosity ratio $M = 1.67$). The water saturation contours, polymer concentration contours and surfactant concentration contours at four different time points of the flooding process have been presented in Figures 22–24 respectively. We observe that with both, the change in the concentration of the injected surfactant and the injected polymer, the method is able to produce qualitatively accurate water saturation, polymer concentration and surfactant concentration contours through the heterogeneous permeability field while showing the intricate details of the advancing fronts.

5 Conclusions

In this work we propose a mathematical model of two-phase, multi-component, incompressible, immiscible flow in porous media that arises in the context of chemical EOR processes, in particular polymer flooding and surfactant-polymer flooding. The mathematical model is a coupled system of an elliptic equation for pressure and parabolic equations for water saturation and concentrations of polymer and surfactant. This model takes into account the capillary pressure. A new global pressure formulation has been developed which

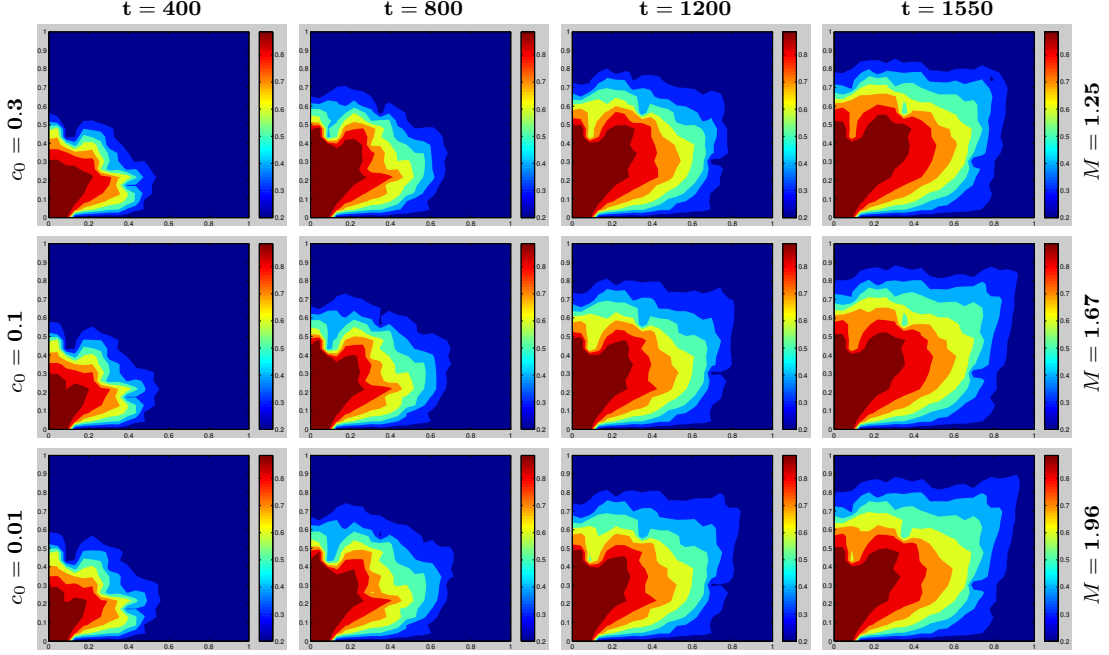


Figure 19: Comparison of water saturation contours in a quarter five-spot reservoir with spatial resolution of 24×24 during three different SP floods. The concentrations of injected polymer in three floods were $c_0 = 0.01, 0.1, 0.3$ with viscosity ratios $M = 1.96, 1.67, 1.25$ respectively. The permeability field used is given in Figure 18. The contours are plotted at four different time levels.

renders the form of the elliptic equation with a discontinuous coefficient to be the same as the one without the capillary pressure included in the model, except for the fact that now we solve the elliptic equation for the global pressure. Using this global pressure variable, the system of flow and transport equations bears some similarity with that of a miscible displacement process which is known to be much simpler to solve numerically. A new hybrid numerical method based on an extended finite element method for discontinuous coefficient elliptic pressure equation and a modified method of characteristics in combination with a time-implicit finite difference method for the transport equations is developed and implemented. Numerical simulations of several polymer and SP floodings through heterogeneous porous matrix have been performed. Numerical results qualitatively show the convergence and robustness of the numerical method.

The numerical simulations were carried out with three different types of heterogeneous permeability fields - piecewise discontinuous with rectangular inclusions, Upper-Ness formation type from the SPE10 problem and a scalar, log-normal permeability field generated using a stationary, isotropic, fractal Gaussian distribution. Two types of piecewise discontinuous permeability fields with one or more square inclusions have been used in simulations. The method has been validated by comparing these numerical results with those available in the literature. The method is able to produce results that show that polymer flooding in comparison to secondary recovery (water flooding) under similar reservoir conditions with heterogeneous Upper-Ness type permeability field data from the SPE10 benchmark problem improves the sweeping efficiency and inhibits growth of fingering instability. Numerical convergence of the method under grid refinement has been shown by performing polymer flood simulations in heterogeneous porous media using three different mesh sizes. The robustness of the method has been further demonstrated by simulating surfactant-polymer floods with various different compositions of the injected surfactant-polymer solution. The method is able to produce fairly well intricate details of the flow heterogeneity and viscosity driven finger formations.

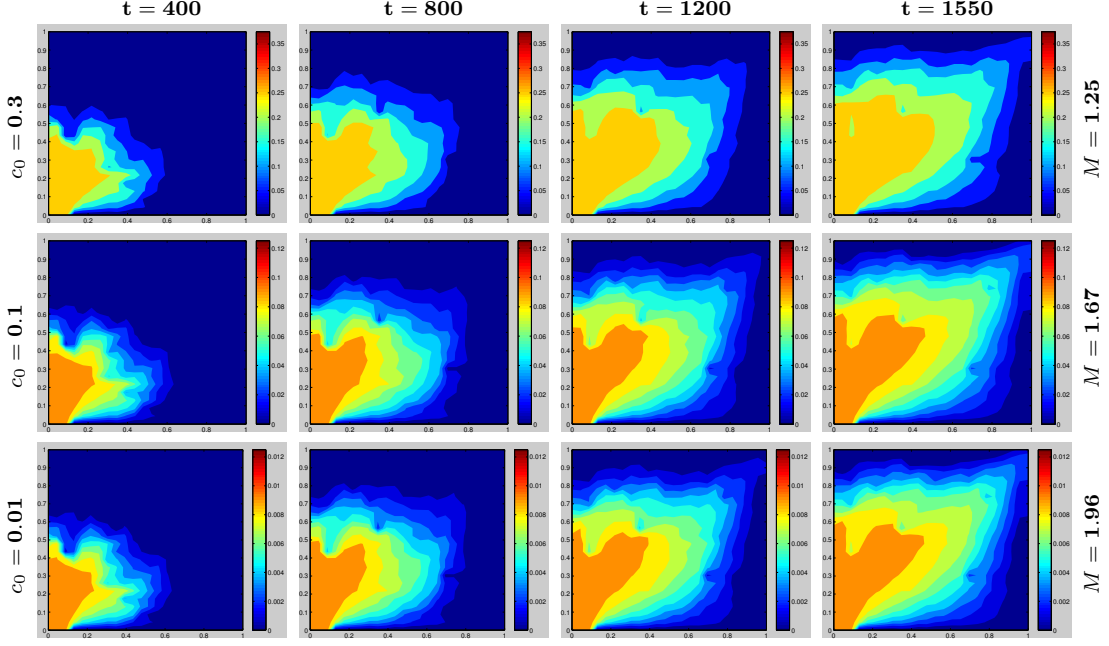


Figure 20: Comparison of polymer concentration contours in a quarter five-spot reservoir with spatial resolution of 24×24 during three different SP floods. The concentration of injected polymer is given by c_0 and M is the viscosity ratio. The permeability field is given in Figure 18. The contours are plotted at four different time levels.

6 Acknowledgement

The work of P.D. was supported in part by the NPRP grant 08-777-1-141 through Qatar National Research Fund and by the U.S. National Science Foundation grant DMS-1522782. The work of S.D. (the student) was supported in part by the NPRP grant 08-777-1-141 through Qatar National Research Fund.

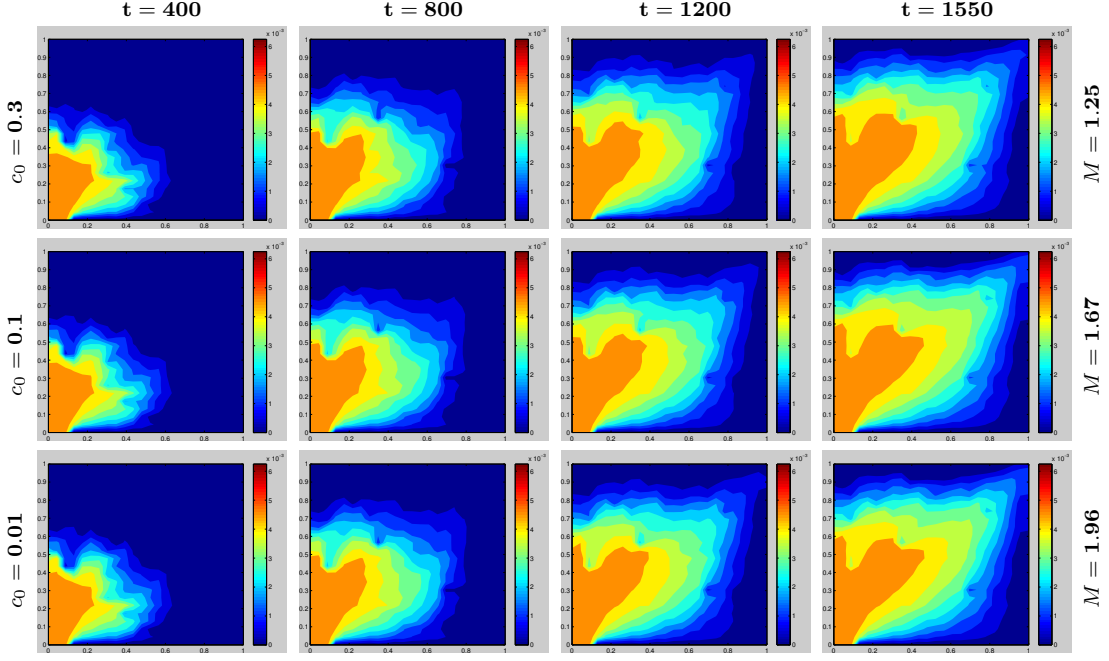


Figure 21: Comparison of surfactant concentration contours in a quarter five-spot reservoir with spatial resolution of 24×24 during three different SP floods. The permeability field used is given in Figure 18. The contours are plotted at four different time levels.

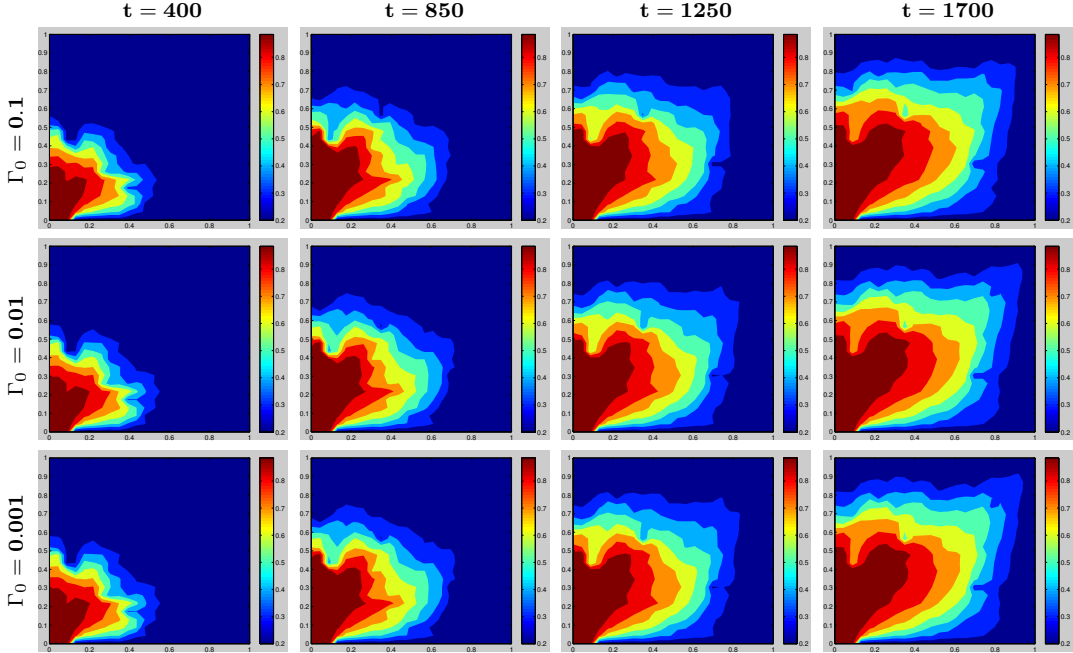


Figure 22: Comparison of water saturation contours in a quarter five-spot reservoir with spatial resolution of 24×24 , during three different SP floods. The surfactant concentrations in the injected fluids in each case were $\Gamma_0 = 0.001, 0.01, 0.1$. The permeability field used is given in Figure 18.

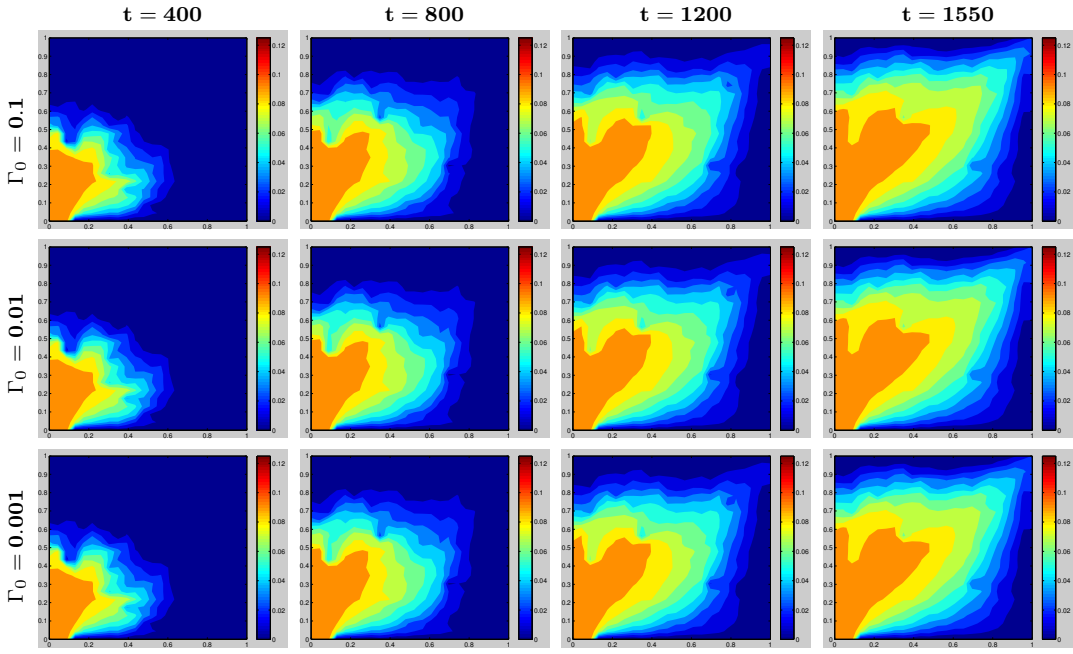


Figure 23: Comparison of polymer concentration contours during three SP floods with different injected surfactant concentrations in a quarter five-spot reservoir with spatial resolution of 24×24 . The contours are plotted at four different time levels.

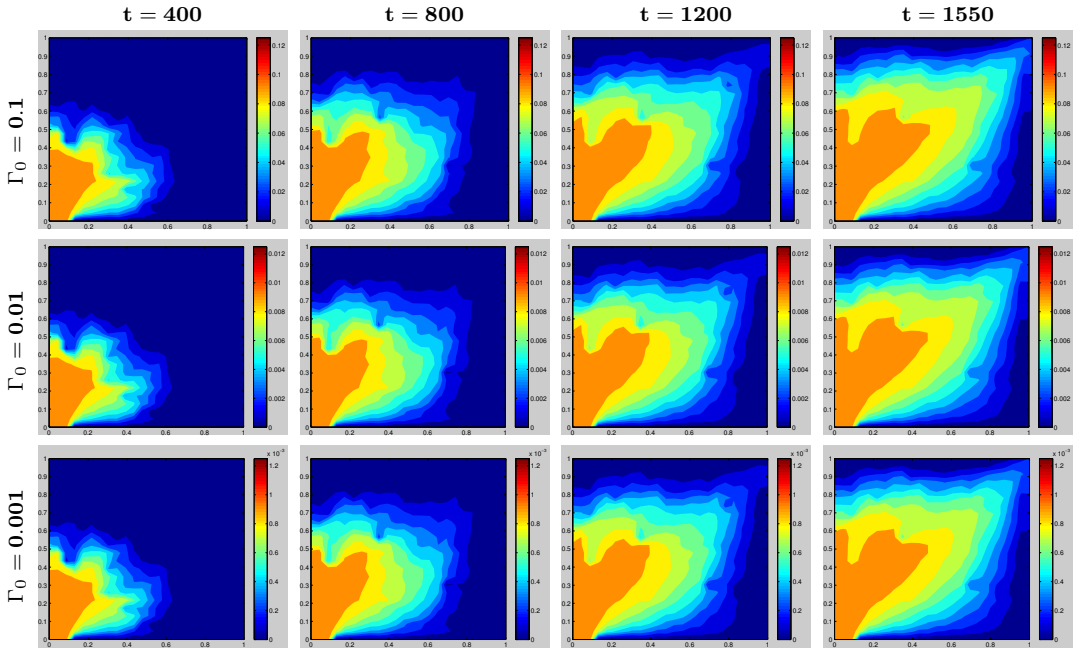


Figure 24: Comparison of surfactant concentration contours during three SP floods with different injected surfactant concentrations in a quarter five-spot reservoir with spatial resolution of 24×24 . The contours are plotted at four different time levels.

References

- Abreu, E. (2014). Numerical modelling of three-phase immiscible flow in heterogeneous porous media with gravitational effects. *Mathematics and Computers in Simulation*, 97:234–259.
- Alsofi, A. M., Liu, J. S., Han, M., and Aramco, S. (2013). Numerical simulation of surfactant-polymer coreflooding experiments for carbonates. *Journal of Petroleum Science and Engineering*, 111:184–196.
- Amaefule, J. O. and Handy, L. L. (1982). Effect of interfacial tensions on relative oil/water permeabilities of consolidated porous media. *Society of Petroleum Engineers Journal*, 22(3):371–381.
- Arbogast, T. and Wheeler, M. F. (1995). A characteristics-mixed finite element method for advection-dominated transport problems. *SIAM Journal on Numerical analysis*, 32(2):404–424.
- Bastian, P. (2003). Higher order discontinuous Galerkin methods for flow and transport in porous media. volume 35 of *Lecture Notes in Computational Science and Engineering*, pages 1–22. Springer Berlin Heidelberg.
- Borges, M. R., Pereira, F., and Amaral Souto, H. P. (2010). Efficient generation of multi-scale random fields: A hierarchical approach. *International Journal for Numerical Methods in Biomedical Engineering*, 26:176–189.
- Brooks, R. H. and Corey, A. T. (1966). Properties of porous media affecting fluid flow. *Journal of the Irrigation and Drainage Division*, 92,(IR2):61–88.
- Brown, C. L. and Pope, G. A. (1994). Simulation of surfactant-enhanced aquifer remediation. *Water Resources Research*, 30(11):2959–2977.
- Celia, M. A., Russell, T. F., Herrera, I., and Ewing, R. E. (1990). An Eulerian-Lagrangian localized adjoint method for the advection-diffusion equation. *Advances in Water Resources*, 13(4):187–206.
- Chavent, G. and Jaffre', J. (1986). *Mathematical Models and Finite Elements for Reservoir Simulation*. Studies in Mathematics and its applications, Amsterdam, North Holland.
- Chen, Z. (2002). Characteristic mixed discontinuous finite element methods for advection-dominated diffusion problems. *Computer Methods in Applied Mechanics and Engineering*, 191(2324):2509–2538.
- Christie, M. A. and Blunt, M. J. (2001). Tenth SPE Comparative Solution Project: A Comparison of Upscaling Techniques. *SPE Reservoir Evaluation & Engineering*, 4(4):308–317.
- Corey, A. T. (1986). *Mechanics of Immiscible Fluids in Porous Media*. Water Resources Publications, Littleton, Colorado.
- Daripa, P., Glimm, J., Grove, J., Lindquist, B., and McBryan, O. (1986). Reservoir simulation by the method of front tracking. In *Proc. of the IFE/SSI seminar on Reservoir Description and Simulation with Emphasis on EOR*, pages 1–18.
- Daripa, P., Glimm, J., Lindquist, B., Maesumi, M., and McBryan, O. (1988a). On the simulation of heterogeneous petroleum reservoirs. In *Numerical Simulation in Oil Recovery*, IMA Vol. Math. Appl. 11, pages 89–103, New York, NY. Springer.
- Daripa, P., Glimm, J., Lindquist, B., and McBryan, O. (1988b). Polymer floods: A case study of nonlinear wave analysis and of instability control in tertiary oil recovery. *SIAM Journal of Applied Mathematics*, 48:353–373.
- Daripa, P. and Pasa, G. (2004). An optimal viscosity profile in enhanced oil recovery by polymer flooding. *International Journal of Engineering Science*, 42(19-20):2029–2039.

- Douglas Jr, J., Frías, D., Henderson, N., and Pereira, F. (2003). Simulation of single-phase multicomponent flow problems in gas reservoirs by Eulerian-Lagrangian techniques. *Transport in Porous Media*, 50(3):307–342.
- Douglas Jr, J., Huang, C.-S., and Pereira, F. (1999). The modified method of characteristics with adjusted advection. *Numerische Mathematik*, 83(3):353–369.
- Douglas Jr, J., Pereira, F., and Yeh, L.-M. (2000). A locally conservative Eulerian-Lagrangian numerical method and its application to nonlinear transport in porous media. *Computational Geosciences*, 4(1):1–40.
- Douglas Jr, J. and Russell, T. F. (1982). Numerical methods for convection-dominated diffusion problems based on combining the method of characteristics with finite element or finite difference procedures. *SIAM Journal on Numerical Analysis*, 19(5):871–885.
- Durlofsky, L. J. (1993). A triangle based mixed finite element-finite volume technique for modeling two phase flow through porous media. *Journal of Computational Physics*, 105(2):252–266.
- Furtado, F. and Pereira, F. (2003). Crossover from Nonlinearity Controlled to Heterogeneity Controlled Mixing in Two-Phase Porous Media Flows. *Computational Geosciences*, 7(2):115–135.
- Gao, C., Shi, J., and Zhao, F. (2014). Successful polymer flooding and surfactant-polymer flooding projects at Shengli oilfield from 1992 to 2012. *Journal of Petroleum Exploration and Production Technology*, 4(1):1–8.
- Ghanbarian-Alavijeh, B., Liaghat, A., Huang, G.-H., and van Genuchten, M. T. (2010). Estimation of the van Genuchten Soil Water Retention Properties from Soil Textural Data. *Pedosphere*, 20(4):456–465.
- Glimm, J., Lindquist, W. B., Pereira, F., and Zhang, Q. (1993). A theory of macrodispersion for the scale-up problem. *Transport in Porous Media*, 13(1):97–122.
- Healy, R. and Russell, T. (1993). A finite-volume Eulerian-Lagrangian localized adjoint method for solution of the advection-dispersion equation. *Water Resources Research*, 29(7):2399–2413.
- Hou, S., Wang, W., and Wang, L. (2010). Numerical method for solving matrix coefficient elliptic equation with sharp-edged interfaces. *Journal of Computational Physics*, 229:7162–7179.
- Islam, M. and Chakma, A. (1991). Mathematical modelling of enhanced oil recovery by alkali solutions in the presence of cosurfactant and polymer. *Journal of Petroleum Science and Engineering*, 5(2):105–126.
- Karazincir, O., Thach, S., Wei, W., Prukop, G., Malik, T., and Dwarakanath, V. (2011). Scale formation prevention during ASP flooding. In *SPE International Symposium on Oilfield Chemistry*. Society of Petroleum Engineers.
- Katsanis, E., Krumrine, P., and Falcone Jr, J. (1983). Chemistry of precipitation and scale formation in geological systems. In *SPE Oilfield and Geothermal Chemistry Symposium*. Society of Petroleum Engineers.
- Li, J. and Rivière, B. (2014). Numerical solutions of the incompressible miscible displacement equations in heterogeneous media. *Computer Methods in Applied Mechanics and Engineering*, 292:107–121.
- Li, Z., Lin, T., and Wu, X. (2003). New cartesian grid methods for interface problems using the finite element formulation. *Numerische Mathematik*, 96:61–98.
- Liu, Q., Dong, M., Ma, S., and Tu, Y. (2007). Surfactant enhanced alkaline flooding for western canadian heavy oil recovery. *Colloids and Surfaces A: Physicochemical and Engineering Aspects*, 293(13):63 – 71.

- Liu, X.-D., Fedkiw, R. P., and Kang, M. (2000). A boundary condition capturing method for Poisson's equation on irregular domains. *Journal of Computational Physics*, 160:151–178.
- Nayagum, D., Schäfer, G., and Mosé, R. (2004). Modelling two-phase incompressible flow in porous media using mixed hybrid and discontinuous finite elements. *Computational Geosciences*, 8(1):49–73.
- Parker, J. C., Lenhard, R. J., and Kuppusamy, T. (1987). A parametric model for constitutive properties governing multiphase flow in porous media. *Water Resources Research*, 23(4):618–624.
- Reed, W. H. and Hill, T. R. (1973). Triangular mesh methods for the neutron transport equation. *Los Alamos Scientific Lab., N.Mex. (USA)*.
- Rivière, B. and Wheeler, M. F. (2002). Discontinuous Galerkin methods for flow and transport problems in porous media. *Communications in Numerical Methods in Engineering*, 18(1):63–68.
- Russell, T. F. and Celia, M. A. (2002). An overview of research on Eulerian-Lagrangian localized adjoint methods (ELLAM). *Advances in Water Resources*, 25(8):1215–1231.
- Shiyi, Y., Puhua, Y., Zhongqiu, D., and Kuiyou, S. (1995). Numerical simulation of alkali/surfactant/polymer flooding. In *International meeting on petroleum engineering*, pages 139–152.
- Thirawarapan, C., Thiele, M. R., Kovsek, A., Batycky, R., and Clemens, T. (2014). A simplified model for field-scale surfactant-polymer flooding. In *SPE Heavy Oil Conference-Canada*. Society of Petroleum Engineers.
- van Genuchten, M. T. (1980). A closed form equation for predicting the hydraulic conductivity of unsaturated soils. *Soil Science Society*, 44:892–898.
- Wang, H., Ewing, R. E., and Russell, T. F. (1995). Eulerian-Lagrangian localized adjoint methods for convection-diffusion equations and their convergence analysis. *IMA journal of numerical analysis*, 15(3):405–459.
- Wu, Z., Yue, X., Cheng, T., Yu, J., and Yang, H. (2014). Effect of viscosity and interfacial tension of surfactant-polymer flooding on oil recovery in high-temperature and high-salinity reservoirs. *Journal of Petroleum Exploration and Production Technology*, 4(1):9–16.
- Yu, Q., Jiang, H., and Zhao, C. (2010). Study of interfacial tension between oil and surfactant polymer flooding. *Petroleum Science and Technology*, 28(18):1846–1854.
- Zhenquan, L., Aimei, Z., Cui, X., Li, Z., Lanlei, G., and Liantao, S. (2012). A successful pilot of dilute surfactant-polymer flooding in Shengli oilfield. In *SPE Improved Oil Recovery Symposium*. Society of Petroleum Engineers.
- Zhu, Y., Zhang, Y., Niu, J., Liu, W., and Hou, Q. (2012). The research progress in the alkali-free surfactant-polymer combination flooding technique. *Petroleum Exploration and Development*, 39(3):371–376.